

1 **Order and disorder in layered double hydroxides: Lessons learned from the green rust**
2 **sulphate - nikischerite series.**

3

4 Knud Dideriksen^{1,2,*}, Laura Voigt^{2,3}, Marco C. Mangayayam², Simon H. J. Eiby², Case M. van
5 Genuchten^{1,4}, Cathrine Frandsen⁵, Kirsten M. Ø. Jensen², S. L. S. Stipp^{5,2} and Dominique J.
6 Tobler²

7

8 ¹Geological Survey of Denmark and Greenland (GEUS), Øster Voldgade 10, 1350 Copenhagen
9 K, Denmark (*Corresponding author: kdi@geus.dk)

10 ²Nano-Science Center, Department of Chemistry, University of Copenhagen, 2100 Copenhagen
11 Ø, Denmark. Previous address for KD, LV, SHJE, and SLSS.

12 ³Department of Chemistry, Technical University of Denmark, 2800 Kgs. Lyngby, Denmark

13 ⁴Department of Earth Sciences, Utrecht University, Netherlands

14 ⁵Department of Physics, Technical University of Denmark, 2800 Kgs. Lyngby, Denmark

15

16

17 **Abstract**

18 Layered double hydroxides (LDHs) occur naturally and are synthesised for catalysis, drug
19 delivery and contaminant remediation. They consist of Me(II)-Me(III) hydroxide sheets
20 separated by hydrated interlayers and weakly held anions. Often, LDHs are nanocrystalline and
21 sheet stacking and Me(II)-Me(III) arrangement can be disordered, which influence reactivity and
22 complicate structural characterisation. We have used pair distribution function (PDF) analysis, to
23 provide detailed information about local and medium range order (≤ 9 nm), to determine the
24 structure of synthetic Fe(II)-Fe(III)/Al(III) LDH. The data are consistent with ordered Me(II)
25 and Me(III) in hydroxide sheets, where structural coherence along the *c* axis decreases with

increasing Al content. The PDF for Fe(II)-Al(III) LDH (nikischerite) is best matched by a pattern for a single metal hydroxide sheet. Parallel to decreased structural coherence between layers, coherence within layers decreased to ~6 nm for synthetic nikischerite. Thus, disorder developed within *and* between the sheets, resulting in mosaic crystals with coherent scattering domains decreasing in all directions. The high density of grain boundary terminations would affect reactivity. Based on classical nucleation theory and the Kossel crystal growth model, we propose that loss of structural coherence stems from increased supersaturation and the presence of Al-hydroxides during formation of the Al-rich LDH.

1. Introduction

Layered double hydroxides (LDH) consist of metal hydroxide layers that contain both divalent and trivalent metals (Me(II) and Me(III)), that are separated by interlayers with loosely held water, anions and sometimes, cations. The metals of the hydroxide layers are octahedrally coordinated, connected by edges, yielding a structure where the metals can be easily substituted. A wide range of Me(II) and Me(III) can be accommodated, at variable ratios.¹ The incorporation of Me(III) in the hydroxide layers results in excess positive charge, that is compensated by intercalation of anions in the hydrated interlayers. Cl⁻, SO₄²⁻, and CO₃²⁻ are the most common anions in synthetic and natural LDHs but more exotic anions can also be intercalated, including larger organic anions. Once intercalated, anions can be replaced by ion exchange, analogous to the cation exchange of silicate clay minerals. The diversity in LDH composition and their anion exchange capacity has attracted considerable attention in materials science, where LDH compounds are investigated for a range of purposes, such as catalysts and catalyst support, vehicles for drug delivery and anion exchangers for environmental remediation.^{e.g., 2, 3, 4, 5}

Although much progress has been made in understanding the nature of LDH and how to manipulate it, several fundamental aspects about its structure are poorly defined and remain controversial. Better understanding of structure and the degree of ordering would improve prediction of LDH properties. Theoretically, the Me(II) and Me(III) in the hydroxide layers can be perfectly ordered at certain Me(II): Me(III) ratios, e.g., 2 and 3, but the actual arrangement has been reported to range from fully ordered⁶ to disordered or outright random.^{e.g., 7, 8} For example, a seminal study interpreted that order developed when Me(II) and Me(III) had comparable ion size⁹ but later work showed that order can also develop in unequally matched Me(II/III) such as Mg(II) and Al(III) in hydrotalcite.¹⁰ Because LDH crystal size is often small and the stacking sequence of the hydroxide layers can be disordered, unambiguous determination of cation ordering is difficult using traditional techniques, such as laboratory based X-ray diffraction.¹¹

Here, we focus on the order and disorder in LDH with Fe(II) and the common trivalent cations, Fe(III) and Al(III). The presence of Fe(II) confers redox reactivity to LDH, making them attractive reactants for reduction of contaminants in environmental engineering and important for understanding natural redox reactions in the Earth sciences. The Fe(II)/Fe(III) variant, green rust (GR), is a product of corrosion¹² and can reduce a range of contaminants thereby immobilising them. Examples include U(VI), Cr(VI) and Np(V).^{13, 14, 15, 16} In addition, chlorinated ethenes, such as trichloroethylene, which pose a significant environmental threat, can be degraded rapidly by green rust in combination with bonechar.¹⁷ GR can form during bacterial iron reduction^{e.g., 18} and its presence in nature has been reported.^{e.g., 19, 20, 21} Laboratory work shows that green rust can reduce nitrate at appreciable rates,²² meaning abiotic nitrogen reduction by GR could be significant in soils and sediments. Finally, experiments indicate that GR is likely to have formed in Archean oceans, with potentially important implications for ancient marine environments.²³

75 The Fe(II)-Al(III) LDH, also known as nikischerite and classified within the wermlandite group,
76 ²⁴ is also redox active²⁵ and can readily form at circumneutral to slightly acidic pH from
77 adsorption of Fe(II) to aluminium oxides and to aluminium containing phyllosilicate clay
78 minerals. ^{26, 27} This suggests that Al(III) and Fe(II) bearing LDH, either as a pure phase or as
79 Al(III) substituted green rust, ^{28, 29} could be quite common at redox boundaries where bacterial
80 iron reduction occurs.

81 Aspects of the redox activity of GR and nikischerite can, however, vary fundamentally. Based
82 on circumstantial experimental evidence, several studies have suggested that electrons are
83 mobile in GR, e.g., ³⁰ similar to what has been observed for Fe(III)-(oxyhydr)oxides. e.g., ^{31, 32}
84 Modelling supports this hypothesis, predicting appreciable electron mobility, in particular within
85 the hydroxide sheet, through hopping as small polarons. ³³ From the perspective of cation
86 ordering in the hydroxide layers, this could mean that the electrons can redistribute themselves
87 during and after synthesis to produce an Fe(II) and Fe(III) distribution, that minimises crystal
88 energy. Aluminium, on the other hand, has no divalent state so its valence would be unaffected
89 by electron mobility and the element would have to resort to diffusion to redistribute in the
90 lattice.

91 The aim of this work was to characterise the order and disorder of LDH with a range of Al(III)
92 in the sodium and sulphate bearing GR - nikischerite series $(\text{NaFe(II)}_6\text{Fe(III)}_x\text{Al(III)}_{3-x}(\text{OH})_{18}(\text{SO}_4)_2 \cdot 12 \text{H}_2\text{O})$, where $0 < x < 3$) and determine the controls on ordering. Materials were
93 synthesised in the laboratory and characterised using synchrotron X-ray pair distribution
94 function analysis, a technique able to resolve material structure even when only local or medium
95 range order exists. The new structural insights were complemented with Mössbauer
96 spectroscopy and transmission electron microscopy (TEM).

98

99 2. Materials and Methods

100 2.1 Synthesis

101 We used an anaerobic chamber (Coy Laboratory Products) for synthesis and sample preparation.
102 Temperature was ~ 26 °C and the N_2/H_2 atmosphere ($H_2 \approx 2\%$) was maintained anoxic using
103 palladium pellets to remove O_2 (< 20 ppm detection limit). Prior to use, all labware was cleaned
104 with 1 M HCl and rinsed three times with deionized water (DI, resistivity = $18.2\text{ M}\Omega\text{cm}$).
105 Reagent grade $0.25\text{ M FeSO}_4 \cdot 7H_2O$, 0.1 M NaOH and $0.25\text{ M Al}_2(SO_4)_3 \cdot 7H_2O$ were used to
106 prepare three stock solutions with DI water, which had previously been deoxygenated by N_2
107 purging for 4 h.

108 All LDH was synthesised following the constant pH oxidation method.³⁴ 150 mL of 0.05 M
109 Fe^{2+} solution was prepared by filtering ($0.22\text{ }\mu\text{m}$) an aliquot of the $FeSO_4 \cdot 7H_2O$ stock solution
110 and diluting it with deoxygenated DI water inside a Teflon beaker. For Al-LDH syntheses, the
111 total cation concentration was kept constant ($nFe^{2+} + nAl^{3+} = 0.05\text{ M}$) but the Al molar fraction
112 of was increased to $x_{Al} = 0.03, 0.1, 0.2$ and 0.33 , with $x_{Al} = nAl^{3+}/(nFe^{2+} + nAl^{3+})$. Oxidation at
113 constant pH 7 was performed by sparging the solution continuously with CO_2 free air (cleaned
114 using a 1 M NaOH trap) and automatic base addition by a titrator system (785 DMP Titrino,
115 Metrohm with Ag/AgCl pH-electrode). For these materials, the onset of Fe(II) bearing LDH
116 formation was visible by the blue-green colour of the suspension. LDH synthesis was complete
117 when the NaOH addition rate suddenly decreased. Based on trial experiments, the synthesis was
118 stopped shortly before this inflection point, to minimise formation of other Fe oxides, such as
119 goethite and magnetite. For $x_{Al} = 0.33$, the synthesis was performed without O_2 oxidation to
120 prevent the formation of Fe(III) and its incorporation in the product. The experiment was
121 terminated when about 16 mL of 1 M NaOH had been titrated to the solution. The resulting
122 suspension was white with a slightly bluish tint. Wet solid samples for characterisation were
123 obtained by centrifugation and removal of the supernatant.

124

125 **2.2 Analytical methods**

126 *Transmission electron microscopy (TEM)*: A small amount of the wet solid was resuspended in
127 deoxygenated DI water. A 3 μ L drop of the suspension was placed on a formvar/carbon coated
128 copper grid and dried for 30 minutes. The specimen was placed in an air-tight container and
129 transported to the TEM (Phillips CM 20) for imaging at an accelerating voltage of 200 kV.

130 *Mössbauer Spectroscopy (MS)*: LDH slurries with approximately 24 g/L Fe were prepared by
131 centrifugation and resuspension in a smaller volume of supernatant. The slurries were put into
132 Plexiglas sample holders and then capped with silicon grease. When ready, the samples were
133 taken out of the anaerobic chamber, quickly shaken and then dropped immediately into liquid
134 nitrogen, to protect the material from oxidation during transport (about 1 hour) to the
135 spectrometer. ^{57}Fe Mössbauer spectroscopy was carried out at 80 K, using constant acceleration
136 spectrometers with ^{57}Co in Rh as the source. The zero point velocity for the spectra was
137 calibrated to that of α -Fe metal. Absorption lines in the spectra were fitted with Lorentzian peak
138 form with line widths and intensities of the absorption pairs constrained to be identical.

139 *Synchrotron pair distribution function (PDF) analyses*: Wet solids were dried inside the
140 anaerobic chamber, crushed with a mortar and pestle and loaded into glass capillaries (0.9 mm
141 inner diameter; Mark Röhrchen). The tubes were sealed with paraffin and placed in airtight
142 containers for transportation to the Advanced Photon Source, Argonne National Laboratory,
143 USA. We demonstrated that highly oxygen sensitive samples remained anoxic for at least 1
144 week when prepared this way. ³⁵ High energy X-ray scattering measurements were made at the
145 11-ID-B beamline (58.6 keV, $\lambda = 0.2114 \text{ \AA}$), using a $40 \times 40 \text{ cm}$ amorphous Si 2D detector
146 (Perkin-Elmer) and a sample-to-detector distance of $\sim 16 \text{ cm}$. A CeO_2 standard was used to
147 calibrate the sample-to-detector distance and the tilt angle with respect to the beam path. In
148 addition to the samples, we measured an empty glass capillary for background correction and a

149 goethite standard for determining the instrument parameters. The 2D data were polarization
150 corrected and azimuthally integrated to 1D scattering patterns using the software Fit-2D.^{36, 37}
151 PDFs were obtained from the scattering patterns using PDFgetX2.³⁸ Standard data processing in
152 PDFgetX2 included background subtraction, normalization, and corrections for angular
153 dependent, nonlinear detector efficiency and incoherent scattering. Because the reduced
154 scattering structure function, $F(Q)$, i.e. $Q[S(Q) - 1]$, for some samples contained spikes at $Q >$
155 22 \AA^{-1} , the Fourier transform included data only to $Q_{\text{max}} = 22 \text{ \AA}^{-1}$. In the data treatment, the
156 composition of the samples was assumed to be $\text{NaFe(II)}_6\text{Fe(III)}_x\text{Al(III)}_{3-x}(\text{OH})_{18}(\text{SO}_4)_2 \cdot 12 \text{ H}_2\text{O}$
157 for the layered double hydroxides, with x derived from the Fe(III)/Fe(II) ratio in Mössbauer
158 spectra or assumed to be 0 for the unoxidised, synthetic nikischerite.

159 *Atomic absorption spectroscopy:* To determine the time dependent decrease in dissolved Fe(II)
160 during LDH synthesis, 0.5 mL samples were removed at regular time steps, centrifuged and the
161 supernatant filtered (0.2 μm) and acidified (2% nitric acid) for subsequent analysis using atomic
162 absorption spectroscopy (AAS, Perkin Elmer AAnalyst 800). The measured absorbance was
163 compared to a series of Fe standards prepared and measured the same way.

164

165 **3. Results and Discussion**

166

167 **3.1 Pair distribution function analysis**

168 Figure 1 depicts the intensity of scattered X-rays as a function of the magnitude of the scattering
169 vector, $I(Q)$, for various $\text{Al(III)}/(\text{Al(III)}+\text{Fe(III)})$ molar ratio in the solid (denoted x_{Al}). Q is
170 inversely related to the spacing between lattice planes, d , with $Q = 2\pi/d$. All samples show
171 pronounced peaks at $Q \approx 0.57, 1.14$ and 1.71 \AA^{-1} , the positions expected for the basal plane
172 reflections for GR ($x_{\text{Al}} = 0$)³⁹ and nikischerite ($x_{\text{Al}} = 0.33$)⁴⁰. With increasing x_{Al} , the peaks

173 broaden somewhat. In contrast, peaks located at $Q \approx 2.35$ to 3.67 \AA^{-1} , which often represent (03 l)
 174 reflections (Figure 1B), substantially decrease in intensity as the proportion of Al increases.
 175 They broaden considerably and shift position. Such preferential decrease in the intensity of many
 176 (0 kl) peaks is expected from disordered stacking along the c axis. ^{e.g., 1, 9}
 177 The first part of the PDF pattern at $r < 11 \text{ \AA}$ largely reflects the structure of the electron dense
 178 metal (Me) hydroxide sheet (Figure 2A) and does not include correlations across the interlayer
 179 from atomic pairs located in different hydroxide layers, which are separated by $\sim 11 \text{ \AA}$. The first
 180 intense peak at $\sim 2.1 \text{ \AA}$ has contributions from first neighbour Me-O pairs. The second intense
 181 peak at $\sim 3.15 \text{ \AA}$ results from first neighbour Me-Me pairs in edge sharing octahedra. Based on
 182 inspection of the structure of the metal hydroxide sheet, the next two peaks at $\sim 4 \text{ \AA}$ and $\sim 5 \text{ \AA}$
 183 stem from Me-O pairs, followed by three intense peaks from Me-Me pairs. These peaks are
 184 present for all samples, a signature of the local bonding environment expected for the LDH
 185 structure. With increase in x_{Al} , many peaks shift position towards lower r , reflecting substitution
 186 of Fe(III) for the smaller cation, Al(III). In addition, a small amount of Al could be present as an
 187 Al hydroxide with coherent scattering domains of a size that make them difficult to detect. An
 188 example of a PDF from a precipitate formed in a solution with only $\text{Al}_2(\text{SO}_4)_3$ is presented in
 189 Figure SI1. This compares with the small peak at $r \approx 2.8 \text{ \AA}$ in the PDF for the sample with $x_{\text{Al}} =$
 190 0.33 (Fig. 2A and B), which corresponds in position to that of the second peak in the precipitate
 191 from $\text{Al}_2(\text{SO}_4)_3$ solutions (Fig. SI1) and to the peak expected for O-O and edge sharing Al-Al
 192 atomic pairs in basaluminite ($\text{Al}_4(\text{OH})_{10}(\text{SO}_4) \cdot 4\text{H}_2\text{O}$).⁴¹ Thus, we cannot fully exclude that a
 193 small amount of basaluminite is present alongside the LDH.
 194 The first intense peak at $\sim 2.1 \text{ \AA}$ (Me-O pairs) broadens with increasing x_{Al} , its maxima shifts to
 195 higher r and a shoulder develops towards lower r (Figure 2B). This shows that several atom
 196 pairs, with differences in r , contribute to the peak, i.e., Fe(II)-O, Fe(III)-O, and Al-O in Al-LDH
 197 samples. Similar distinct Me-O distances in LDH have been observed previously with X-ray

198 absorption spectroscopy^{e.g., 9} and PDF. ⁴² To deconvolute the first Me-O peak into 2 (for GR) and
 199 3 components (for Al-LDH), Gaussian fitting was applied, minimising the sum of squared
 200 residuals between measured and calculated patterns (Figure 2B; method in Supplementary
 201 Information). In the fitting, the effects on the PDF from the sloping base line, instrument
 202 dampening and size of coherent scattering domains were ignored. To constrain the fit, the peak
 203 for LDH with $x_{\text{Al}} = 0$ was first fit with two Gaussian shaped contributions, where relative areas
 204 were constrained to 2.3, based on the Fe(II)/Fe(III) ratio determined with MS (ignoring slight
 205 differences in electron density of Fe(II) and Fe(III)). Next, the pattern for nikischerite with $x_{\text{Al}} =$
 206 0.33 was fit with three Gaussian contributions where position and FWHM of the Fe
 207 contributions were set to the values determined for pure GR but their intensity was optimised. In
 208 addition, the position of the Al-O contribution was set to 1.895 Å based on the ionic radii
 209 presented by Shannon⁴³ for octahedrally coordinated Al and O in threefold coordination and the
 210 peak intensity and FWHM was fit. Finally, the PDFs for GR with $x_{\text{Al}} = 0.03, 0.1,$ and 0.2 were
 211 fit by setting positions and FWHM's to those already derived and allowing only intensity to vary.

 212 The 2-component fit for GR gave distances of 2.13 Å for Fe(II)-O and 2.00 Å for Fe(III)-O,
 213 which agree well with data from Shannon⁴³ as well as the peak positions for Fe(II)(OH)₂³⁵ and a
 214 range of Fe(III) oxides⁴⁴. For Al-LDH samples, where the Al-O distance was constrained to
 215 1.895 Å ⁴³, the FWHM for the three Me-O pairs decreased with a decrease in cation radius, with
 216 values for the Gaussian peaks of 0.26 Å for Fe(II)-O, 0.24 Å for Fe(III)-O and 0.17 Å for Al-O.
 217 This suggests that thermal or static atomic displacement of oxygen atoms affects the longer and
 218 weaker Fe(II)-O bond more, which is reasonable. Finally, the calculated Fe(III)/Fe(II) ratios
 219 from the area of the Gaussian peaks are consistent with those determined from Mössbauer
 220 spectroscopy (Figure 2D; Figure SI2; Table SI1).

 221 For the second intense peak in the PDF, representing first neighbour Me-Me distance, a single
 222 Gaussian contribution fits the peaks well (Fig. 2B) and yields peak positions decreasing from

223 3.17 Å for $x_{\text{Al}} = 0$ to 3.12 Å for $x_{\text{Al}} = 0.33$, correlating with the Al/Fe(II) ratio derived from the
224 PDF data (Figure SI3). This shows that the structural changes induced by Al incorporation
225 during synthesis are systematic. The FWHM derived from the fitting changes slightly with
226 increasing x_{Al} , from ~ 0.24 Å for GR to ~ 0.25 Å for intermediate Al-Fe(III) LDH and ~ 0.23 Å for
227 nikischerite (Fig. 2C). Although the width represents both thermal and static atomic
228 displacement, the trend is consistent with intermediate x_{Al} resulting in some disorder in the
229 hexagonal pattern of the metals. This would be expected for substitution involving two
230 differently sized ions.

231 The changes in Me-Me distance and peak width suggests that the Me part of the lattice contracts
232 fairly uniformly in response to Al incorporation, with some disorder for intermediate x_{Al} ,
233 whereas the marked changes of the Me-O distance indicate that oxygen in the hydroxyl becomes
234 substantially displaced. Given the Me-O and Me-Me distances, we can determine the distance
235 between O atoms that link two edge sharing metals, based on Heron's formula⁴⁵ (details in
236 Figure SI4). Calculations for Fe(III)-Fe(II) and Al(III)-Fe(II) configurations yield O-O distances
237 of 2.64 Å and 2.53 Å, i.e. a decrease in the O-O distance for O atoms that coordinate Al(III) to a
238 value approaching the expected 2.44 Å for closest packing, from ionic radius from Shannon.⁴³
239 For an ideal LDH structure, where all O atoms are identically coordinated within the hydroxide
240 sheet (i.e. to one Me(III) and two Me(II), ignoring weaker bonding to interlayer atoms),
241 shortening of O-O distance would most likely occur by contraction of the sheet along the c axis
242 as well as by rotation of the top and bottom O-triads of the Me(II) octahedra to bring the O
243 atoms closer to each other. Such a model is consistent with that proposed by Bellotto et al.⁹
244 However, if the metals are randomly positioned but at Me-Me distances from the PDF fitting, O-
245 O distances for Al(III)-Al(III) configurations would have to be very short, 2.14 Å.

246 In the full PDF, the pattern for the GR with $x_{\text{Al}} = 0$ has peaks from atoms with correlated
247 positions up to ~ 90 Å (Figure 3). Compared with the pattern measured for a well crystalline

248 goethite standard, this decay in peak intensity primarily reflects instrument resolution. As Al
249 content increases, the oscillations extend to progressively shorter distances, reflecting a decrease
250 in the size of the coherent scattering domains, as low as ~ 60 Å for $x_{\text{Al}} = 0.33$. At r values ranging
251 from 12 - 26 Å, where peaks from atom pairs in different Me hydroxide sheets contribute to the
252 pattern, the PDFs also show very distinct differences with increasing x_{Al} (Figure 4). Peak
253 positions are offset to lower r for the Al-LDH, reflecting contraction of the crystal structure, and
254 some peaks show very large changes in intensity, whereas others do not, suggesting that the
255 progressive structural alterations are anisotropic. Given the appearance of the $I(Q)$ (Fig. 1), this
256 most likely reflects disarray of the arrangement of hydroxide sheets in the c direction because of
257 stacking disorder. To assess the impact of stacking disorder along the c axis on PDFs at
258 $r > 11$ Å, the PDF of a single Fe(II)-Fe(III) hydroxide sheet with a diameter of 6 nm was
259 calculated with the software DiffPy-CMI,⁴⁶ based on the structure by Christiansen et al.³⁹, and
260 subtracted by the PDF calculated for a bulk GR crystal (red line with superposed fat dashed line
261 in Fig. 4). This calculated differential PDF (i.e., single sheet - bulk crystal) corresponds well
262 with the difference in PDFs between experimental samples with $x_{\text{Al}} = 0.33$ and $x_{\text{Al}} = 0$. Thus,
263 both intra- and intersheet structural coherence decreases as x_{Al} increases. At $x_{\text{Al}} = 0.33$, the
264 sample has very little structural coherence between layers and the coherence within the metal
265 hydroxide layer is on the order of 6 nm.

266

267 3.2 Interpreting the changes in structural coherence

268 Several aspects of the material could lead to the observed decrease in structural coherence.
269 Particle size, for example, might be very small, with dimensions similar to those determined for
270 the coherent scattering domains. TEM images of the materials are shown in Figure 5. GR
271 samples show well developed hexagonal particles with an average width of ~ 300 nm. With
272 increasing x_{Al} , average particle width decreases to about ~ 40 nm for $x_{\text{Al}} = 0.33$. At this Al

273 content, particles were sometimes observed in an upright position in the images (example in
274 insert of Fig. 5D), allowing measurement of particle thickness, which ranges from about 4 to 10
275 nm. Clearly, the width and thickness of particles are much larger than the dimensions of the
276 coherent scattering domains from PDF.

277 Pair distribution function analysis of glassy carbon has shown that sheet bending in layered
278 solids can result in significant decrease in the dimensions of the coherent scattering domains
279 within the sheets.^{47, 48} Upright particles in TEM images sometimes display bending with a
280 radius of curvature of about 100 nm (example in insert in Fig. 5D). To determine if such bending
281 could explain our observations, PDFs were calculated for variably curved, 18 nm wide single Me
282 hydroxide sheets with $x_{Al} = 0.33$, using the nikischerite structure.⁴⁰ Appreciable changes in the
283 calculated PDF occur only at a radius of curvature of about 12.5 nm (Figure SI5). Such a radius
284 of curvature would mean that the average particle, if composed of a domain as wide as the
285 particles, would have to curl back on itself to produce a nanotube. Although GR has been
286 observed to form nanotubes,⁴⁹ we did not observe them in these experiments. Thus, particle
287 curvature cannot explain the observed decrease in structural coherence within the metal
288 hydroxide sheet.

289 Previous studies using PDF have shown that static disorder in crystals results in broader peaks
290 and more extensive decay of peak intensity with increasing r , than would be expected from ideal
291 materials.^{50, 51} To probe if the peaks in measured PDFs are different in width from those
292 expected for an ideal structure, calculated PDFs based on three structural models with ordered
293 distribution of Me(II) and Me(III) were fit to the data for the end member samples, i.e. where x_{Al}
294 = 0 and $x_{Al} = 0.33$, using the software PDFgui⁵² and DiffPy-CMI⁴⁶. Details about the structures
295 and the fitting are given in the Supplementary Information, Section 2.

296 The PDFgui fits for a bulk crystal for the sample with $x_{Al} = 0$ are shown in Figure 6 and Table
297 SI2. Residuals of the fit are presented in Figure SI8. Both models yield realistic values for fitting

parameters, including larger displacement parameters, U_{iso} , for interlayer atoms. This has also been observed for intercalated iodide⁴² and the calculated and measured patterns agree reasonably well, with a simpler P 3 model achieving better agreement for low r peaks and slightly poorer agreement for higher r compared to the model by Christiansen et al.³⁹. For the sample with $x_{\text{Al}} = 0.33$, which showed very little structural coherence across interlayers, fitting was performed in two steps. First, the Huminicki and Hawthorne⁴⁰ and the P 3 bulk structures were fit in PDFGui to the data, ranging from 1.7 - 10 Å, where correlations across interlayers did not contribute. Based on these results, the structure for single Me-hydroxide sheets, 6 nm wide were constructed and fit using DiffPy-CMI. For both structures, the calculated patterns were very similar, agreed reasonably with the measurements and gave realistic values for the fitting parameters (Fig. 6 and Table SI2). Although both patterns showed some discrepancy from the measured PDF, measured peaks are not systematically broadened as r values increased compared with those expected for the ideal, calculated structures. Thus, the PDF showed no resolvable signs of disorder in the atomic arrangement within the Me hydroxide sheet, that could explain the observed decrease in the length scale of the structural coherence.

313

314 **3.3 Structural coherence: Implications and causes**

Modelling suggests that electrons are mobile in GR, hopping as thermally activated, small polarons between Fe atoms.³³ Alternatively, intervalence charge transfer has been proposed to be responsible for the green-blue colour of LDH,⁵³ as for other iron bearing minerals.⁵⁴ Regardless of whether electron transfer is caused thermally or by absorption of light, Fe(II) and Fe(III) might rearrange to give an ordered Me(II)-Me(III) distribution within the metal hydroxide layer. Indeed, high resolution AFM shows a pattern with superstructures, where periodicities are consistent with an ordered arrangement of Fe(II) and Fe(III) in the hydroxide layer.³⁹ In contrast, for Al-bearing samples, reordering of Me(II)-Me(III) would require

diffusion of Al(III) if initial ordering is not achieved. Thus, a hypothesis at the outset of our work was that incorporation of Al in the Me hydroxide layer might give rise to disorder in cation distribution. Our PDF data indicate increased Me-Me distances at intermediate x_{Al} , but short distances for the endmembers with $x_{\text{Al}} = 0$ and 0.33 (Figure 2). Given that AFM data indicate Fe(II) and Fe(III) ordering for $\text{GR}_{\text{Na}, \text{SO}_4}$, the variation of Me-Me distances suggests that both endmembers are ordered but that coexistence of both Fe(III) and Al(III) causes structural relaxation. The satisfactory fitting of the endmember PDFs substantiates this interpretation. Thus, we interpret that both $\text{GR}_{\text{Na}, \text{SO}_4}$ and nikischerite have a high degree of cation ordering at local and intermediate range. Hence, our data neither confirms nor contests that electrons are mobile in green rust.

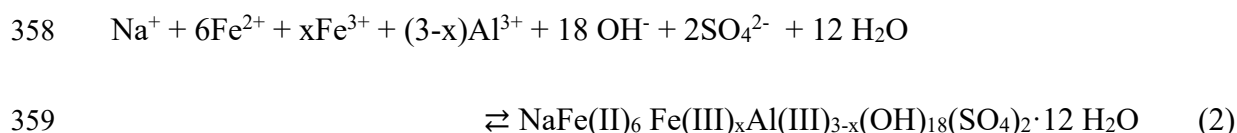
Our data indicate that structural coherence decreases both within layers and between them as the Al content increases. Lack of structural coherence between layers, i.e., stacking disorder, arises easily in layered materials, such as silicate clays and carbon, which have strong bonds within layers and much weaker bonds between layers. For LDH, the translation of structure from one hydroxide layer to the next is generally considered to occur largely through hydrogen bonds between the hydroxyl groups of the metal hydroxyl layer, the water and ions in the interlayer.⁵⁵ Mapping the strength and directionality of the hydrogen bond network is no simple task. As a first approximation, the smaller size of Al(III) should render it more polarising, resulting in stronger hydrogen bonds from the hydroxyl groups. Using the dynamics of water shells coordinating to Me ions as an analogue, Al(III) possesses slower exchange kinetics for water in the first shell than Fe(III)⁵⁶ and it is among the highly polarising Me(III) that have strong hydrogen bonding from the first shell water to those of the second shell. e.g.,^{57, 58} Based on modelling, this results in approximately 4 times longer residence time for second shell water bonding to Al(III) than for Fe(III).⁵⁹ Thus, it is not clear that substitution of Al(III) in the hydroxide sheets would weaken hydrogen bonding and facilitate disarray in the stacking order,

nor that it would cause concomitant decrease in the length for the structural coherence within the hydroxide layers.

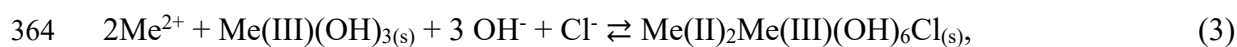
In the absence of obvious causes from crystallography and crystal chemistry for the coupled loss of coherence along all crystallographic axes, we turned to aspects of how the materials formed, i.e. nucleation and growth. These processes are controlled by several aspects of the system, such as the surface free energy at the interfaces and the presence of foreign ions and particles, ^{e.g., 60} but they depend critically on the supersaturation, Ω :

$$\Omega = \frac{IAP}{K_{sp}}, \quad (1)$$

where K_{sp} refers to the solubility product and IAP to the product of the actual activities of the ions, both with reference to the reaction:



A study of the relative stability of a range of Fe(III) and Al(III) LDH with interlayer chloride indicates that the Al(III) versions are more stable than the Fe(III) counterparts with respect to their Me(III) hydroxides). ⁶¹ For a simplified reaction equation:



they determined equilibrium constants for LDH that were ~1000 fold higher on average for the Al(III) LDH, reflecting higher solubility for Al(III) hydroxides. In our experiments, the source of Al(III) is nanocrystalline basaluminite and the Fe(III) activity is unlikely to have greatly exceeded ferrihydrite solubility. Given that the bulk pH and Fe(II) concentration in all our experiments are the same, these considerations indicate that the Al-rich LDH most likely formed at significantly higher saturation state, Ω . A higher stability of Al(III)-bearing LDH with respect

371 to Me(III)-(oxyhydr)oxides should entail lower aqueous Fe(II) concentrations, i.e. a shift in
372 equilibrium toward products in Eq. 3. Consistent with this, the Fe(II) concentration determined
373 during LDH formation and subsequent oxidation to Me(III)-(oxyhydr)oxides was lower for the
374 material produced at $x_{\text{Al}} = 0.12$ than for $x_{\text{Al}} = 0$ (Figure SI9).

375 Higher Ω in experiments containing Al(III) and the presence of nanocrystalline basaluminite
376 would be expected to have had several implications:

377 1. Nucleation rate for crystals increases with increasing supersaturation ^{e.g., 60, 62, 63}; details on the
378 rates of nucleation in the Supplementary Information, Section 3). Thus, LDH with smaller
379 particle sizes should have formed in experiments with higher x_{Al} , where Ω was most likely
380 higher. Moreover, nucleation in the experiments with Al(III) occurred in the presence of
381 basaluminite particles, which could act as a substrate for faster heterogeneous nucleation of
382 LDH, if interfacial tension is favourable. If so, even more, smaller LDH particles would have
383 formed. These considerations are consistent with our TEM images (Figure 5), which show
384 decreasing particle size with increasing x_{Al} .

385 2. The manner by which crystals grow is also affected by the value of Ω . The Kossel model of a
386 crystal surface consists of flat terraces, steps linking adjacent terraces and kinks on the steps. ⁶⁴
387 At these three types of growth sites, attachment of ions to produce growth occurs progressively
388 faster and requires decreasing values of Ω . ^{e.g., 60} Hence, growth at kinks and steps occurs quickly
389 until the active sites here are depleted. Establishment of growth on top of a terrace requires
390 nucleation of a new layer through a process akin to regular nucleation (termed 2D nucleation;
391 details in SI Section 3). Similar to crystal nucleation, the rate of 2D nucleation increases with Ω .
392 The process can also be favoured by the presence of foreign particles on the surface of a growing
393 crystal when surface free energies favour wetting of the foreign particle by the 2D nucleus.
394 Thus, the presence of nanocrystalline basaluminite might well have decreased the energy barrier
395 (and rate) for 2D nucleation.

396 3. In general, increased Ω means that formation of metastable, and sometimes disordered phases,
397 become possible. Examples of disordered phases include dense liquids^{e.g., 65} and amorphous
398 solids (e.g. amorphous calcium carbonate⁶⁶). For Mg-Al LDH, high temperature oxide melt
399 solution calorimetry indicates that stacking faults produce a solid that is metastable with respect
400 to the ordered material,⁶⁷ with faults originating from kinetic reasons. Thus, the faster reaction
401 rates that are expected as Ω increases with x_{Al} , could mean that lack of structural coherence in
402 the direction of stacking would develop.

403 Taken together, these considerations indicate that the increased Ω and the presence of foreign
404 particles in experiments with Al(III) could well result in rapid nucleation of particles and growth
405 characterised by more numerous 2D nucleation events, producing 2D islands that i) are
406 structurally incoherent with respect to the layer beneath and to each other and ii) grow until
407 pinned by other islands. The outcome of this would be small particles, consisting of sheets with
408 decreased structural coherence lengths, both internally and between sheets, as we observe.

409 Generally, the Kossel model for crystal growth predicts a shift from spiral growth, where steps
410 and kinks are generated continuously at low supersaturation, to growth by 2D nucleation at
411 higher saturation. e.g. ⁶⁰ Growth spirals have recently been observed for Zn-Al LDH grown at low
412 supersaturation. ⁶⁸ Our results suggest that growth of LDH in general conforms to the
413 expectation from the Kossel model, with 2D nucleation taking place at higher saturation. In
414 addition, our results suggest that the weak bonding between sheets in LDH allows for nucleation
415 and growth of 2D islands that are an isolated structurally coherent entity, leading to formation of
416 mosaic crystals. Such crystals would have a high density of internal grain boundaries, where
417 surface termination at the LDH edges could be highly reactive.⁶⁹

418

419 **Acknowledgements**

420 This work was partly funded by the European Union's Horizon 2020 Research and Innovation
421 Programme Metal-Aid (Marie Skłodowska-Curie grant agreement No. 675219). D.J.T.
422 acknowledges financial support from MIRO (PIEF-GA-2013-624619), a Marie Curie Intra-
423 European Fellowship (IEF). This research used resources of the Advanced Photon Source, a U.S.
424 Department of Energy (DOE) Office of Science User Facility operated for the DOE Office of
425 Science by Argonne National Laboratory under Contract No. DE-AC02-06CH11357. D.J.T and
426 K.D. are thankful for assistance provided during beam time from Olaf Borkiewicz and Kevin A.
427 Beyer at APS beamline 11 ID-B, APS, and for financial support for travels to APS from the
428 Danish Council for Independent Research (via DANSCATT).

429

430

431 **References**

432 (1) Drits, V. A.; Bookin A. S. Crystal Structure and X-Ray Identification of Layered Double
433 Hydroxides. In *Layered Double Hydroxides: Present and Future*; Rives V., Ed.; Nova Science
434 Publishers: New York, **2001**; pp. 41-100.

435 (2) Li, F.; Duan, X. Applications of Layered Double Hydroxides. In *Structure and bonding*,
436 *119*; Duan X. and Evans D. G., Eds: Springer Berlin: Heidelberg, **2006**; pp 193–223.

437 (3) Roeffaers, M. B. J.; Sels, B. F.; Uji-i, H.; De Schryver, F. C.; Jacobs, P. A.; De Vos, D.
438 E.; Hofkens, J. Spatially resolved observation of crystal-face-dependent catalysis by single
439 turnover counting. *Nature* **2006**, 439, 572–575.

440 (4) Fan, G.; Li, F.; Evans, F. G.; Duan, X. Catalytic applications of layered double
441 hydroxides: recent advances and perspectives. *Chem. Soc. Rev.* **2014**, 43, 7040-766.

- 442 (5) Islam, Md. S.; Kim, M.; Jin, X.; Oh, S. M.; Lee, N.-S.; Kim, H.; Hwang S.-J.
443 Bifunctional 2D Superlattice Electrocatalysts of Layered Double Hydroxide–Transition Metal
444 Dichalcogenide Active for Overall Water Splitting. *ACS Energy Lett.* **2018**, 3, 952–960.
- 445 (6) Jayanthi, K.; Vishnu Kamath, P. Observation of cation ordering and anion-mediated
446 structure selection among the layered double hydroxides of Cu(II) and Cr(III). *Dalton Trans.*
447 **2013**, 42, 13220–13230.
- 448 (7) Funnell, N. P.; Wang, Q.; Connor, L.; Tucker, M. G.; O'Hare, D.; Goodwin, A. L.
449 Structural characterisation of a layered double hydroxide nanosheet. *Nanoscale* **2014**, 6, 8032–
450 8036.
- 451 (8) Radha, A. V.; Vishnu Kamath, P.; Shivakumara, C. Order and disorder among the
452 layered double hydroxides: combined Rietveld and DIFFaX approach. *Acta Cryst. B* **2007**, 63,
453 243–250.
- 454 (9) Bellotto, M.; Rebours, B.; Clause, O.; Lynch, J.; Bazin, D.; Elkaïm, E. A Reexamination
455 of Hydrotalcite Crystal Chemistry. *J. Phys. Chem.* **1996**, 100, 8527–8534.
- 456 (10) Sideris, P. J.; Nielsen, U. G.; Gan, Z.; Grey, C. P. Mg/Al Ordering in Layered Double
457 Hydroxides Revealed by Multinuclear NMR Spectroscopy. *Science* **2008**, 321, 113–117.
- 458 (11) Hofmeister, W.; Von Platen, H. Crystal Chemistry and Atomic Order in Brucite-related
459 Double-layer Structures. *Crystallogr Rev.* **1992**, 3, 3–26.
- 460 (12) Refait, P.; Memet, J. B.; Bon, C.; Sabot, R.; Génin, J.-M. R. Formation of the Fe(II)–
461 Fe(III) hydroxysulphate green rust during marine corrosion of steel. *Corros. Sci.* **2003**, 45, 833–
462 845.

- 463 (13) O'Loughlin, E. J.; Kelly, S. D.; Csencsits, R.; Cook, R. E.; Kemner, K. M. Reduction of
464 uranium(VI) by mixed iron(II)/iron(III) hydroxide (green rust): Formation of UO₂ nanoparticles.
465 *Environ. Sci. Technol.* **2003**, 37, 721–727.
- 466 (14) Bond, D. L.; Fendorf, S. Kinetics and Structural Constraints of Chromate Reduction by
467 Green Rusts. *Environ. Sci. Technol.* **2003**, 37, 2750-2757.
- 468 (15) Skovbjerg, L. L.; Stipp, S. L. S.; Utsunomiya, S.; Ewing, R. C. The Mechanisms of
469 Reduction of Hexavalent Chromium by Green Rust Sodium Sulphate: Formation of Cr-Goethite.
470 *Geochim. Cosmochim. Acta* **2006**, 70, 3582-3592.
- 471 (16) Christiansen, B. C.; Geckeis, H.; Marquardt, C. M.; Bauer, A.; Römer, J.; Wiss, T.;
472 Schild, D.; Stipp, S. L. S. Neptunyl (NpO₂⁺) interaction with green rust, GR_{Na,SO4}. *Geochim. et*
473 *Cosmochim. Acta* **2011**, 75, 1216–1226.
- 474 (17) Ai, J.; Yin, W.; Hansen, H. C. B. Fast Dechlorination of Chlorinated Ethylenes by Green
475 Rust in the Presence of Bone Char. *Environ. Sci. Technol. Lett.* **2019**, 6, 191-196.
- 476 (18) Ona-Nguema, G.; Abdelmoula, M.; Jorand, F.; Benali, O.; Géhin, A.; Block, J. C.;
477 Génin, J.-M. R. Iron(II,III) Hydroxycarbonate Green Rust Formation and Stabilization from
478 Lepidocrocite Bioreduction. *Environ. Sci. Technol.* **2002**, 36, 16–20.
- 479 (19) Trolard, F.; Bourrié, G.; Abdelmoula, M.; Refait, P.; Feder, F. Fougerite, a new mineral
480 of the pyroaurite–iowaite group: description and crystal structure. *Clays Clay Min.* **2007**, 55,
481 323-334.
- 482 (20) Christiansen, B. C.; Balic-Zunic, T.; Dideriksen, K.; Stipp, S. L. S. Identification of
483 Green Rust in Groundwater. *Environ. Sci. Technol.* **2009**, 43, 3436–3441.

- 484 (21) Zegeye, A.; Bonneville, S.; Benning, L. G.; Sturm, A.; Fowle, D. A.; Jones, C. A.;
485 Canfield, D. E.; Ruby, C.; MacLean, L. C.; Nomosatryo, S.; Crowe, S. A.; Poulton, S. W. Green
486 rust formation controls nutrient availability in a ferruginous water column. *Geology* **2012**, 40,
487 599-602.
- 488 (22) Hansen, H. C. B.; Koch, C. B.; Nancke-Krogh, H.; Borggaard, O. K.; Sørensen, J.
489 Abiotic Nitrate Reduction to Ammonium: Key Role of Green Rust. *Environ. Sci. Technol.* **1996**,
490 30, 2053-2056.
- 491 (23) Halevy, I.; Alesker, M.; Schuster, E.M.; Popovitzbiro, R.; Feldman, Y. A key role for
492 green rust in the Precambrian oceans and the genesis of iron formations. *Nature Geoscience*
493 **2017**, 10, 135-139.
- 494 (24) Mills, S. J.; Christy, A. G.; Génin, J.-M. R.; Kameda, T.; Colombo, F. Nomenclature of
495 the hydrotalcite supergroup: natural layered double hydroxides. *Min. Mag.* **2012**, 76, 1289-1336.
- 496 (25) Zhong, Y.; Yang, Q.; Luo, K.; Wu, X.; Li, X.; Liu, Y.; Tang, W.; Zeng, G.; Peng, B.
497 Fe(II)–Al(III) layered double hydroxides prepared by ultrasound-assisted co-precipitation
498 method for the reduction of bromate. *J. Hazard. Mater.* **2013**, 250-251, 345– 353.
- 499 (26) Elzinga, E. J. Formation of Layered Fe(II)–Al(III)-Hydroxides during Reaction of Fe(II)
500 with Aluminum Oxide. *Environ. Sci. Technol.* **2012**, 46, 4894–4901.
- 501 (27) Zhu, Y.; Elzinga, E. J. Formation of Layered Fe(II)-Hydroxides during Fe(II) Sorption
502 onto Clay and Metal-Oxide Substrates. *Environ. Sci. Technol.* **2014**, 48, 4937–4945.
- 503 (28) Aissa, R.; Ruby, C.; Gehin, A.; Abdelmoula, M.; Génin, J.-M. R. Synthesis by
504 Coprecipitation of Al-Substituted Hydroxysulphate Green Rust. *Hyperfine Interact.* **2004**,
505 156/157, 445-451.

- 506 (29) Ruby, C.; Abdelmoula, M.; Aissa, R.; Medjahdi, G.; Brunelli, M.; François, M.
507 Aluminium Substitution in iron(II-III)-Layered Double Hydroxides: Formation and Cationic
508 Order. *J. Solid State Chem.* **2008**, 181, 2285-2291.
- 509 (30) Refait, P.; Abdelmoula, M.; Génin, J.-M. R. Mechanisms of formation and structure of
510 green rust one in aqueous corrosion of iron in the presence of chloride ions. *Corros. Sci.* **1998**,
511 39, 1547-1560.
- 512 (31) Yanina, S. V.; Rosso, K. M. Linked reactivity at mineral–water interfaces through bulk
513 crystal conduction. *Science* **2008**, 320, 218–222.
- 514 (32) Katz, J. E.; Zhang, X.; Attenkofer, K.; Chapman, K. W.; Frandsen, C.; Zarzycki, P.;
515 Rosso, K. M.; Falcone, R. W.; Waychunas, G. A.; Gilbert, B. Electron small polarons and their
516 mobility in iron (oxyhydr)oxide nanoparticles. *Science* **2012**, 337, 1200-1203.
- 517 (33) Wander, M. C. F.; Rosso, K. M.; Schoonen, M. A. A. Structure and Charge Hopping
518 Dynamics in Green Rust. *J. Phys. Chem. C* **2007**, 111, 11414-11423.
- 519 (34) Schwertmann, U.; Fechter, H. The Formation of Green Rust and Its Transformation to
520 Lepidocrocite. *Clay Miner.* **1994**, 29, 87-92.
- 521 (35) Dideriksen, K.; Frandsen, C.; Bovet, N.; Wallace, A.; Sel, O.; Arbour, T.; Navrotsky, A.;
522 De Yoreo, J. J.; Banfield, J. F. Formation and transformation of a short range ordered iron
523 carbonate precursor. *Geochim. Cosmochim. Acta* **2015**, 164, 94-109.
- 524 (36) Hammersley, A. P.; Svensson, S. O.; Thompson, A. Calibration and correction of spatial
525 distortions in 2D detector systems. *Nucl. Instr. Meth.* **1994**, A346, 312–321.
- 526 (37) Hammersley A. P. FIT2D: An Introduction and Overview. *ESRF Internal Report* **1997**,
527 ESRF97HA02T. Available at http://www.esrf.eu/computing/scientific/FIT2D/FIT2D_

- 528 (38) Qiu, X.; Thompson, J. W.; Billinge, S. J. L. PDFgetX2: A GUI-Driven Program to
529 Obtain the Pair Distribution Function from X-Ray Powder Diffraction Data. *J. Appl. Crystallogr.*
530 **2004**, 37, 110-116.
- 531 (39) Christiansen, B. C.; Balic-Zunic, T.; Petit, P. O.; Frandsen, C.; Mørup, S.; Geckeis, H.;
532 Katerinopoulou, A.; Stipp, S. L. S. Composition and Structure of an Iron-Bearing Layered
533 Double Hydroxide (LDH) - Green Rust Sodium Sulphate. *Geochim. Cosmochim. Acta* **2009**, 73,
534 3579-3592.
- 535 (40) Huminicki, D. M. C.; Hawthorne, F. C. The crystal structure of nikischerite,
536 $\text{NaFe}^{2+}_6\text{Al}_3(\text{SO}_4)_2(\text{OH})_{18}(\text{H}_2\text{O})_{12}$, a mineral of the shigaite group. *Can. Mineral.* **2003**, 41, 79-82.
- 537 (41) Carrero, S.; Fernandez-Martinez, A.; Pérez-López, R.; Lee, D.; Aquilanti, G.; Poulain,
538 A.; Lozano, A.; Nieto, J.-M. The nanocrystalline structure of basaluminite, an aluminum
539 hydroxide sulfate from acid mine drainage. *Am. Min.* **2017**, 102, 2381–2389.
- 540 (42) Aimoz, L.; Taviot-Guého, C.; Churakov, S. V.; Chukalina, M.; Dähn, R.; Curti, E.;
541 Bordet, P.; Vespa, M. Anion and cation order in iodide-bearing Zn/Mg-Al layered double
542 hydroxides. *J. Phys. Chem. C* **2012**, 116, 5460–5475.
- 543 (43) Shannon, R. D. Revised Effective Ionic Radii and Systematic Studies of Interatomic
544 Distances in Halides and Chalcogenides. *Acta Cryst. A* **1976**, 32, 751-767.
- 545 (44) Michel F. M.; Ehm L.; Antao S. M.; Lee P. L.; Chupas P. J.; Liu G.; Strongin D. R.;
546 Schoonen M. A. A.; Phillips B. L.; Parise J. B. The Structure of Ferrihydrite, a Nanocrystalline
547 Material. *Science* **2007**, 316, 1726-1729.
- 548 (45) Raifaizen, C. H. A Simpler Proof of Heron's Formula. *Math. Mag.* **1971**, 44, 27-28.

- 549 (46) Juhás, P.; Farrow, C. L.; Yang, X.; Knox, K. R.; Billinge, S. J. L. Complex modeling: a
550 strategy and software program for combining multiple information sources to solve ill posed
551 structure and nanostructure inverse problems. *Acta Cryst. A* **2015**, 562–568.
- 552 (47) Jurkiewicz, K.; Duber, S.; Fischer, H. E.; Burian, A. Modelling of glass-like carbon
553 structure and its experimental verification by neutron and X-ray diffraction. *J. Appl. Cryst.* **2017**,
554 50, 36–48.
- 555 (48) Mathiesen, J. K.; Väli, R.; Härmas, M.; Lust, E.; von Bülow, J. F.; Jensen, K. M. Ø.;
556 Norby P. Following the in-plane disorder of sodiated hard carbon through operando total
557 scattering. *J. Mater. Chem. A* **2019**, 7, 11709–11717.
- 558 (49) Johnson, C. A.; Murayama, M.; Küsel, K.; Hochella, Jr. M. F. Polycrystallinity of Green
559 Rust Minerals and Their Synthetic Analogs: Implications for Particle Formation and Reactivity
560 in Complex Systems. *Am. Min.* **2015**, 100, 2091-2105.
- 561 (50) Petkov, V.; Jeong, I. K.; Chung, J. S.; Thorpe, M. F.; Kycia, S.; Billinge, S. J. L. High
562 real-space resolution measurement of the local structure of Ga_{1-x}In_xAs using X-ray diffraction.
563 *Phys. Rev. Let.* **1999**, 83, 4089-4092.
- 564 (51) Gilbert, B.; Huang, F.; Zhang, H.; Waychunas, G. A.; Banfield, J. F. Nanoparticles:
565 Strained and Stiff. *Science* **2004**, 205, 651-654.
- 566 (52) Farrow, C. L.; Juhás, P.; Liu, J. W.; Bryndin, D.; Božin, E. S.; Bloch, J.; Proffen, Th.;
567 Billinge, S. J. L. PDFfit2 and PDFgui: computer programs for studying nanostructure in crystals.
568 *J. Phys.: Condens. Matter* **2007**, 19, 7 ppp, doi:10.1088/0953-8984/19/33/335219.
- 569 (53) Hansen, H. C. B. Composition Stabilization and Light Absorption of Fe(II)Fe(III)
570 Hydroxycarbonate ('Green Rust'). *Clay Miner.* **1989**, 24, 663-669.

- 571 (54) Allen, G. C.; Hush, N. S. Intervalence-Transfer Absorption. Part 1. Qualitative Evidence
572 for Intervalence-Transfer Absorption in Inorganic Systems in Solution and in the Solid State.
573 *Prog. Inorg. Chem.* **1967**, 8, 357-389.
- 574 (55) Radha, A. V.; Vishnu Kamath, P.; Shivakumara, C. Conservation of Order, Disorder, and
575 “Crystallinity” during Anion-Exchange Reactions among Layered Double Hydroxides (LDHs)
576 of Zn with Al. *J. Phys. Chem. B* **2007**, 111, 3411-3418.
- 577 (56) Helm, L.; Merbach, A. E. Water exchange on metal ions: experiments and simulations.
578 *Coord. Chem. Rev.* **1999**, 187, 151-181.
- 579 (57) Bergström, P.-Å.; Lindgren, J. Infrared Spectroscopic Evidence for Second-Sphere
580 Hydration in Aqueous Solutions of Al^{3+} , Cr^{3+} , and Rh^{3+} . *J. Phys. Chem.* **1991**, 95, 7650-7655.
- 581 (58) Bleuzen, A.; Foglia, F.; Furet, E.; Helm, L.; Merbach, A. E.; Weber, J. Second
582 Coordination Shell Water Exchange Rate and Mechanism- Experiments and Modeling on
583 Hexaaquachromium(III). *J. Am. Chem. Soc.* **1996**, 118, 12777-12787.
- 584 (59) Hofer, T. S.; Weiss, A. K. H.; Randolph, B. R.; Rode, B. M. Hydration of highly charged
585 ions. *Chem. Phys. Lett.* **2011**, 512, 139–145.
- 586 (60) De Yoreo, J. J.; Vekilov, P. G. Principles of Crystal Nucleation and Growth. *Rev.*
587 *Mineral. Geochem.* **2003**, 54, 57-93.
- 588 (61) Bocclair, J. W.; Braterman, P. S. Layered Double Hydroxide Stability. 1. Relative
589 Stabilities of Layered Double Hydroxides and Their Simple Counterparts. *Chem. Mater.* **1999**,
590 11, 298-302.
- 591 (62) Kashchiev, D.; van Rosmalen, G. M. Nucleation in solutions revisited. *Cryst. Res.*
592 *Technol.* **2003**, 38, 555 – 574.

- 593 (63) Vekilov, P. G. Nucleation. *Cryst. Growth Des.* **2010**, 10, 5007–5019.
- 594 (64) Kossel, W. Zur Theorie des Kristallwachstums. *Nachr. Akad. Wiss. Göttingen Math.-*
 595 *Phys. Kl. II* **1927**, 135-143.
- 596 (65) Vekilov, P. G. Dense Liquid Precursor for the Nucleation of Ordered Solid Phases from
 597 Solution. *Cryst. Growth Des.* **2004**, 4, 671-685.
- 598 (66) Brecevic, L.; Nielsen, A. E. Solubility of amorphous calcium carbonate. *J. Cryst. Growth*
 599 **1989**, 98, 504-510.
- 600 (67) Shivaramaiah, R.; Navrotsky, A. Energetics of Order–Disorder in Layered Magnesium
 601 Aluminum Double Hydroxides with Interlayer Carbonate. *Inorg. Chem.* **2015**, 54, 3253–3259.
- 602 (68) Forticaux, A.; Dang, L.; Liang, H.; Jin, S. Controlled Synthesis of Layered Double
 603 Hydroxide Nanoplates Driven by Screw Dislocations. *Nano Lett.* **2015**, 15, 3403–3409.
- 604 (69) Mariano, R. G.; McKelvey, K.; White, H. S.; Kanan, M. W. Selective increase in CO₂
 605 electroreduction activity at grain-boundary surface terminations. *Science* **2017**, 358, 1187–1192.

606

607 **Figure captions**

608 Figure 1. A) I(Q) of samples synthesised with variable Al content (x_{Al}). B) Zoom of I(Q) to show
 609 peaks from $Q = 2$ to 4.5 \AA^{-1} . Peaks are assigned (hkl) based on the structure for GR(Na,SO₄) given
 610 by Christiansen et al.³⁹

611 Figure 2. A) PDF peaks in the r range $0\text{--}12 \text{ \AA}$ with indications of the atomic pairs contributing
 612 dominantly to peak intensity. B) The first neighbour Me-O and Me-Me peak and the Gaussian

613 fitting (grey: individual components; black: sum of components). C) Me-Me peak widths ex-
614 pressed as the full width at half maximum intensity as a function of x_{Al} . D) Fe(III)/Fe(II) ratio at
615 varying x_{Al} derived from fitting the PDF with Gaussian shaped contributions (B) and measured
616 with MS.

617 Figure 3. PDFs for interatomic distance, r , ranging from 0-100 Å. The short, black lines indicate
618 the approximate size of the coherent scattering domains.

619 Figure 4. Zoom of PDFs in the r range 12-26 Å and differential PDFs between i) the patterns
620 measured for $x_{Al} = 0.33$ and $x_{Al} = 0$ (grey line) and i) the calculated patterns for a single green rust
621 sheet and a bulk green rust crystal (red striped line). The coordination number for Fe-Fe pairs
622 within layers are given as black numbers and those between layers, as grey numbers. Measured
623 and calculated patterns have been normalised to give same intensity for the first Me-Me peak at
624 about 3.15 Å.

625 Figure 5. TEM of LDH with $x_{Al} = 0, 0.03, 0.1$ and 0.33 . All scale bars represent 100 nm. Insert in
626 Figure 5D showing bending particle. The uncertainty represents that associated with the average
627 width of particles at 2 standard errors. One standard error equals the standard deviation divided
628 by the number of observations (n).

629 Figure 6. Measured and calculated patterns after fitting crystal models to the data for A)
630 GR(Na,SO₄) ($x_{Al} = 0$) and B) nikisherite ($x_{Al} = 0.33$).

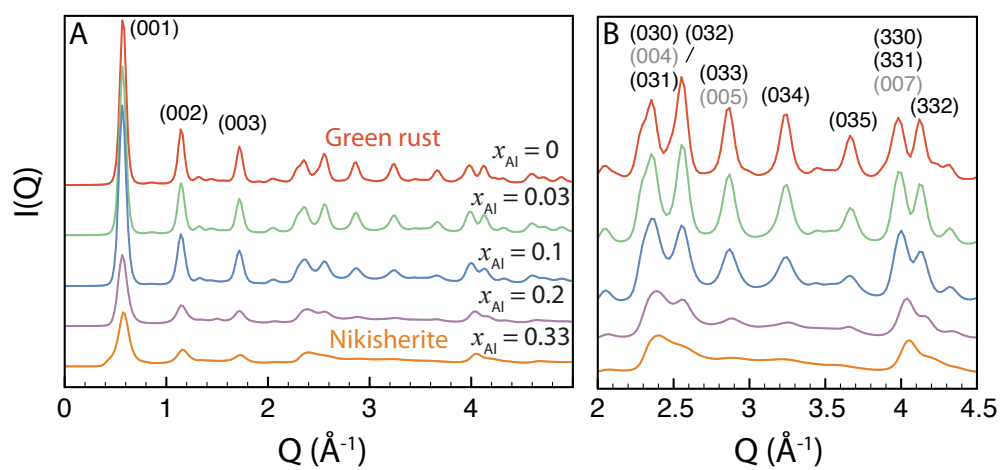


Figure 1

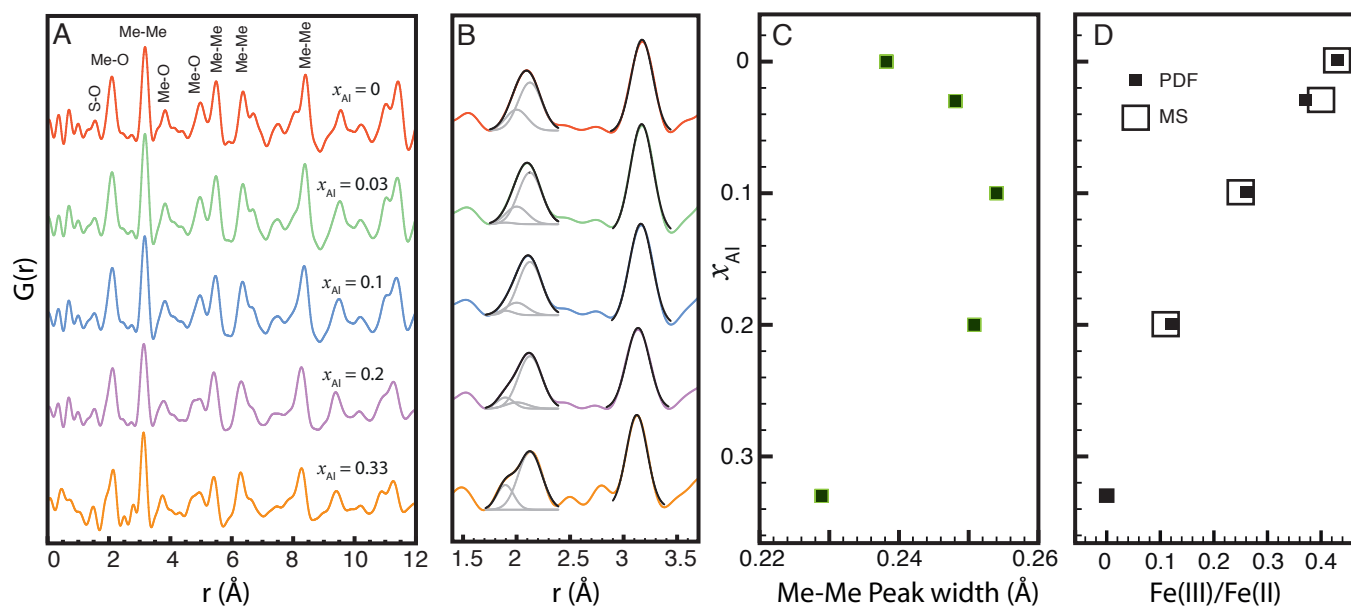


Figure 2

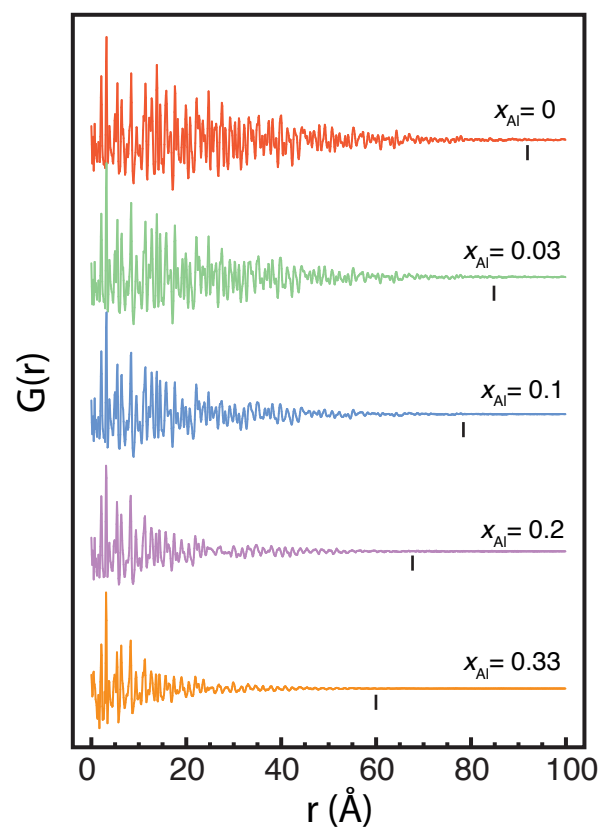


Figure 3

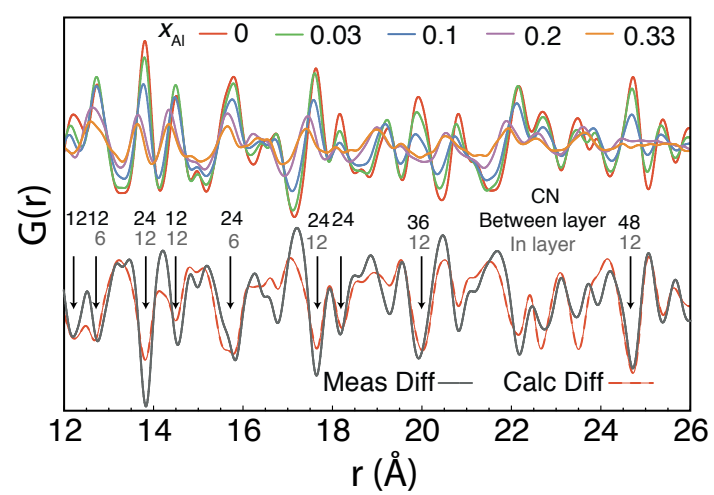


Figure 4

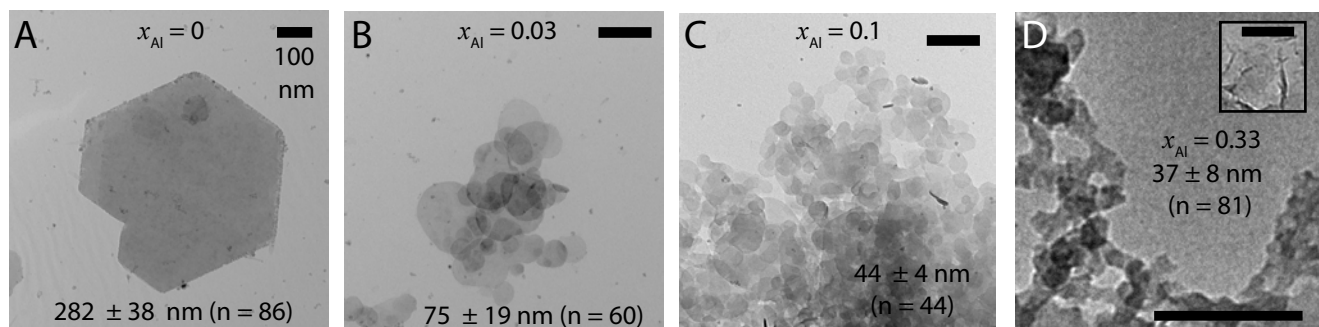


Figure 5

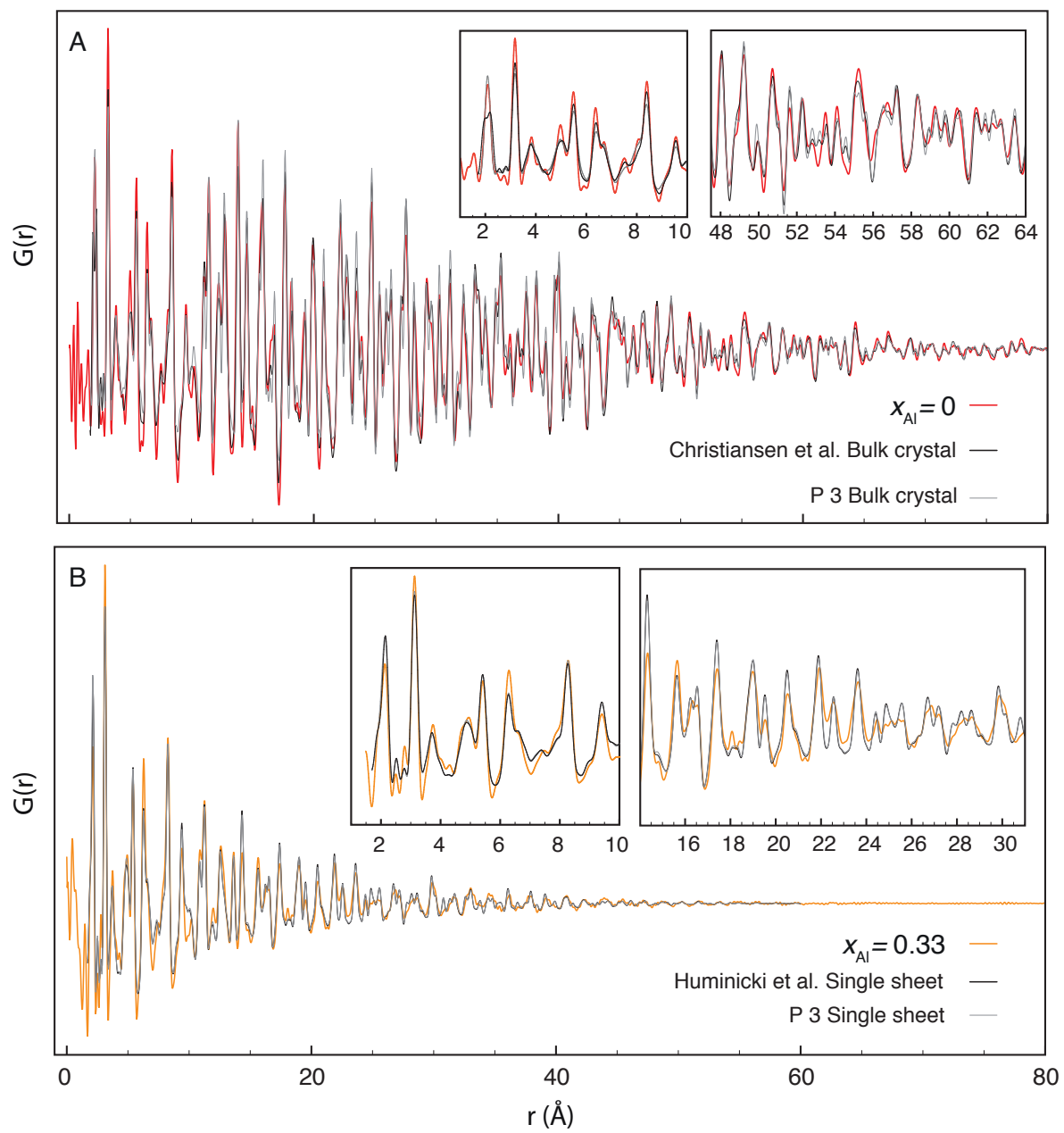


Figure 6

SUPPLEMENTARY INFORMATION

Order and disorder in layered double hydroxides: Lessons learned from the green rust sulphate - nikischerite series.

Knud Dideriksen^{1,2,*}, Laura Voigt^{2,3}, Marco Mangayayam², Simon H. J. Eiby², Case M. van Genuchten^{1,4}, Cathrine Frandsen⁵, Kirsten M. Ø. Jensen², Susan L. S. Stipp^{2,5} and Dominique J. Tobler²

¹Geological Survey of Denmark and Greenland (GEUS), Øster Voldgade 10, 1350 Copenhagen K, Denmark (*Corresponding author: kdi@geus.dk)

²Nano-Science Center, Department of Chemistry, University of Copenhagen, 2100 Copenhagen Ø, Denmark. Previous address for KD, LV, SHJE, and SLSS.

³Department of Chemistry, Technical University of Denmark, 2800 Kgs. Lyngby, Denmark

⁴Department of Earth Sciences, Utrecht University, Netherlands

⁵Department of Physics, Technical University of Denmark, 2800 Kgs. Lyngby, Denmark

Content of the supporting information

The supporting information contains text with details about 1) the methods used for fitting the Mössbauer spectra and the results, 2) the crystal structures and methods employed in the fitting of the pair distribution functions as well as the results; and 3) a description of the theory for classical nucleation and 2D nucleation. In addition, it contains two tables and nine figures.

1. Mössbauer Spectroscopy (MS)

All MS spectra were fit with two doublets for Fe(II) (D_1) and Fe(III) (D_2) (Figure SI2), and their relative abundances, RA , was used to determine the Fe(II):Fe(III) ratio (Table SI1). In the pure GR sample, additional peaks from a magnetically ordered phase were observed, which were fitted with a sextet, S_1 , yielding MS parameters characteristic of goethite (Table SI1).¹ With increasing x_{Al} , a decrease in the spectral area for the D_2 component for Fe(III) was observed, showing a decrease in Fe(III) content with Al(III) substitution. Additionally, a broadening of the D_1 component (i.e. FWHM of Fe^{II}) was observed (Table SI1) with increasing Fe(II) content and Al(III) substitution. The Fe(III):Fe(II) ratio obtained for pure GR is 0.43 and compares well with the values reported in the literature for GR_{SO_4} , which range from 0.43 to 0.53.^{e.g., 2-4}

2. Details about the fitting of the pair distribution functions (PDFs) for $x_{Al} = 0$ and $x_{Al} = 0.33$

For each PDF, we used 1) the corresponding model derived from structural refinement of powder or single crystal XRD^{5,6} and 2) a simple common model based on P 3 symmetry. The structural model for nikischerite, $NaFe(II)_6Al(III)_3(OH)_{18}(SO_4)_2 \cdot 12 H_2O$, is rhombohedral, space group R-3, and has unit cell dimensions, $a \approx 9.35 \text{ \AA}$ and $c \approx 33 \text{ \AA}$.⁶ The unit cell encompasses three metal hydroxide layers and features distinct positions for interlayer SO_4^{2-} and Na^+ , reflecting a highly ordered material. Green rusts with sulphate show variation in both the spacing between hydroxide layer and the cation removability that depend on the identity of the monovalent cation, consistent with cations being placed in the interlayer.⁴ The model for the Green rusts with sulphate and sodium ($GR(Na,SO_4)$;

NaFe(II)₆Fe(III)₃(OH)₁₈(SO₄)₂·12 H₂O) was derived using the nikischerite model as a starting point.⁵ Because of stacking disorder of interlayer ions, the GR(Na,SO₄) model features a smaller trigonal cell, space group P-3, with $a \approx 9.53$ Å and $c \approx 11$ Å that encompass only a single hydroxide sheet. In this model, SO₄²⁻ and Na⁺ are placed in the interlayer space above and below all Fe(III) sites with an occupancy of 1/3, reflecting the lack of ordering of interlayer ions across metal hydroxide sheets. In addition, sulphate tetrahedra are rotated 30° compared to nikischerite structure, so that oxygen atoms at the tetrahedra base are oriented towards the neighbouring Fe(II) atoms, rather than being located almost directly above the top oxygens in the Me(III) octahedra (illustrated in Fig. SI6). To have a model where the positions of the O atoms in the metal hydroxide sheet could be more easily fitted, a simpler structure was constructed based on P 3 symmetry with either Fe(III) or Al(III) as the trivalent metal. In this model, the oxygens of the Me-hydroxide sheet are located in two planes (i.e., identical z position) and the sulphate tetrahedra are located like for GR(Na,SO₄). Details about the P 3 structures are given below. For all models, the top and bottom oxygen triads of the Fe(II) octahedra are rotated with respect to each other to allow shorter Me(III)-O bonds (Fig. SI6). The model parameters were fitted to decrease the squared residual between calculated and measured PDF using PDFGui (bulk crystals) and DiffPy-CMI (single sheets). For all fits, parameters included a scaling factor, a parameter to describe correlated atomic motion (δ_2), the cell dimensions, and a set of isotropic displacement parameters (U_{iso}) for Fe(II), Me(III), O in the hydroxide sheet, O in the interlayer, Na, and S. For the P 3 models, the positions of the oxygens in the metal hydroxide sheet were also refined in both PDFGui and DiffPy-CMI fits, each top and bottom triad constrained to have

identical Me-O bond distance and O-O-O angles of 60 degrees. The P3 structure features two types of oxygen atoms, O1 and O2. To impose the three fold rotational symmetry operating on O1 and O2 in DiffPy-CMI calculations, two displacement vectors (v) were fitted and imposed on the x and y positions of O1 and O2 as well as their symmetry equivalents after vector rotation by angle θ equalling 120° and 240° (Fig. SI7).

P 3 structure for green rust ($x_{Al} = 0$)

```
data_Crystal
_audit_creation_method      'generated by CrystalMaker X for macOS'
_cell_length_a              5.495000
_cell_length_b              5.495000
_cell_length_c              10.970000
_cell_angle_alpha           90.000000
_cell_angle_beta            90.000000
_cell_angle_gamma           120.000000

_symmetry_space_group_name_H-M  'P 3'

loop_
_symmetry_equiv_pos_as_xyz
'+x,+y,+z'
'-y,+x-y,+z'
'-x+y,-x,+z'
```

95 loop_
96 _atom_site_label
97 _atom_site_type_symbol
98 _atom_site_occupancy
99 _atom_site_fract_x
100 _atom_site_fract_y
101 _atom_site_fract_z
102 Me3 Fe 1.0 0.0 0.0 0.5
103 Me2 Fe 1.0 0.6666 0.3333 0.5
104 O1 O 1.0 0.317 0.0 0.59
105 O2 O 1.0 0.0 0.683 0.41
106 Me2 Fe 1.0 0.3333 0.6666 0.5
107 S1 S 0.33333299 0.0 0.0 0.8851
108 S2 S 0.33333299 0.0 0.0 0.1149
109 Na Na 0.33333299 0.0 0.0 0.0
110 OW1 O 0.33333299 0.4 0.2 0.17
111 OW2 O 0.33333299 0.2 0.4 0.83
112 OSO4_1 O 0.33333299 0.0 0.0 0.9778
113 OSO4D O 0.33333299 0.28 0.15 0.1798
114 OSO4_2 O 0.33333299 0.0 0.0 0.0222
115 OSO4D O 0.33333299 0.15 0.28 0.8202
116 OW3 O 0.33333299 0.2 0.35 0.1515
117 OW4 O 0.33333299 0.8 0.65 0.8485
118
119
120

```

121  P 3 structure for nikischerite ( $x_{\text{Al}} = 0.33$ )
122  data_Crystal
123  _audit_creation_method      'generated by CrystalMaker X for macOS'
124  _cell_length_a              5.436000
125  _cell_length_b              5.436000
126  _cell_length_c              10.970000
127  _cell_angle_alpha           90.000000
128  _cell_angle_beta            90.000000
129  _cell_angle_gamma           120.000000
130
131  _symmetry_space_group_name_H-M  'P 3'
132
133  loop_
134  _symmetry_equiv_pos_as_xyz
135  '+x,+y,+z'
136  '-y,+x-y,+z'
137  '-x+y,-x,+z'
138
139  loop_
140  _atom_site_label
141  _atom_site_type_symbol
142  _atom_site_occupancy
143  _atom_site_fract_x
144  _atom_site_fract_y
145  _atom_site_fract_z
146  Me3 Al 1.0 0.0 0.0 0.5

```

147	Me2	Fe	1.0	0.6666	0.3333	0.5
148	O1	O	1.0	0.3	0.0	0.5838
149	O2	O	1.0	0.0	0.7	0.4162
150	Me2	Fe	1.0	0.3333	0.6666	0.5
151	S1	S	0.33333299	0.0	0.0	0.8851
152	S2	S	0.33333299	0.0	0.0	0.1149
153	Na	Na	0.33333299	0.0	0.0	0.0
154	OW1	O	0.33333299	0.4	0.2	0.17
155	OW2	O	0.33333299	0.2	0.4	0.83
156	OSO4_1	O	0.33333299	0.0	0.0	0.9778
157	OSO4D	O	0.33333299	0.28	0.15	0.1798
158	OSO4_2	O	0.33333299	0.0	0.0	0.0222
159	OSO4D	O	0.33333299	0.15	0.28	0.8202
160	OW3	O	0.33333299	0.2	0.35	0.1515
161	OW4	O	0.33333299	0.8	0.65	0.8485
162						
163						

164 Table SI1: Parameters obtained by fitting MS spectra obtained at 80 K.

x_{Al}		δ mm/s	Δ mm/s	FWHM mm/s	RA (%)	Fe(III) / Fe(II)
0	D ₁	1.28	2.91	0.32	64.3	0.43
	D ₂	0.46	0.43	0.29	27.8	
	S ₁	0.48	-0.03	0.46	7.9	
0.03	D ₁	1.28	2.88	0.35	71.6	0.4
	D ₂	0.46	0.45	0.31	28.4	
0.1	D ₁	1.28	2.80	0.39	79.9	0.25
	D ₂	0.46	0.46	0.28	20.1	
0.2	D ₁	1.27	2.67	0.45	90.4	0.11
	D ₂	0.45	0.51	0.25	9.6	

165 δ isomer shift, Δ quadrupole splitting, RA relative abundance

166

167 Table SI2. Parameter value obtained from fitting of the PDFs for material from synthesis
 168 with $x_{Al} = 0$ and $x_{Al} = 0.33$.

	$x_{Al} = 0$		$x_{Al} = 0.33$	
Structure	Christiansen et al.	P 3	Huminicki and Hawthorne	P 3
Fitting type	Bulk structure	Bulk structure	Single sheet	Single sheet
δ_2 (\AA^2)	2.8	2.8	3.6	3.6
a (\AA)	9.53	5.50	9.38	5.42
c (\AA)	10.95	10.94	-	-
$U_{iso}Me(II)$ (\AA^2)	0.007	0.008	0.008	0.008
$U_{iso}Me(III)$ (\AA^2)	0.007	0.006	0.003	0.001
$U_{iso}O(OH)$ (\AA^2)	0.017	0.021	0.017	0.022
$U_{iso}Interlayer O$ (\AA^2)	0.061	0.13	-	-
$U_{iso}S$ (\AA^2)	0.036	0.027	-	-
$U_{iso}Na$ (\AA^2)	0.045	0.021	-	-
Reduced chi squared	0.11	0.12	0.08	0.06

169

170

3. Rates of crystal nucleation and 2D nucleation

The nucleation rate (J) of crystals is classically described by: ⁷⁻⁹

$$J = A \exp\left(\frac{\Delta G'_{\text{nucl}}}{kT}\right),$$

(SI 1)

where A is a preexponential factor related to the addition rates of monomers, the site density for nucleation and the probability for growth of a nucleus at the top of the energy barrier ($\Delta G'_{\text{nucl}}$), whose magnitude for a simplified spherical nucleus is given by:

$$\Delta G'_{\text{nucl}} = \frac{16\pi\gamma_{\text{cw}}^3 V^2}{3(kT\ln(\Omega))^2}.$$

(SI 2)

Here, γ_{cw} signifies the surface energy between cluster and water, V , the molecular volume of the nucleating substance, k , the Boltzmann constant ($1.38 \times 10^{-23} \text{ J K}^{-1}$), and T , absolute temperature. Eqs. SI 1 and SI 2 are such that nucleation rate increases with increasing supersaturation and that a threshold value for Ω exists, above which nucleation rates become significant.

In the presence of a foreign surface, nucleation may occur heterogeneously. For heterogenous nucleation of a hemispherical nucleus on a flat surface, the energy barrier ($\Delta G'_{\text{nucl(Het)}}$) is given by:

$$\Delta G'_{\text{nucl(het)}} = \frac{8\pi\gamma'^3 V^2}{3(kT\ln(\Omega))^2},$$

(SI 3)

where γ' , denotes the effective surface free energy of the nuclei, which is given by:

$$\gamma' = \gamma_{\text{cw}} \left(1 - \frac{\gamma_{\text{SW}} - \gamma_{\text{CS}}}{2\gamma_{\text{cw}}}\right).$$

(SI 4)

Here, γ_{sw} and γ_{cs} denotes the surface free energy between substrate and water, and cluster and substrate. Different geometries of the nucleus and the substrate results in variation in the mathematical expression for nucleation, e.g.,¹⁰ but its dependence on saturation remains unchanged. Depending on the values of the surface free energy of the interfaces, heterogeneous nucleation may greatly increase nucleation rates.

Within the Kossel crystal growth model, establishment of a new layer on top of a terrace requires 2D nucleation, the energy barrier for which is given by:

$$\Delta G'_{2Dnuc} = \frac{h\pi\gamma_{cw}^2 V}{kT \ln(\Omega)},$$

(SI 5)

where h is the step height of the new layer. e.g.,¹¹ Inspection of this equation shows that the energy barrier decreases with Ω , meaning that rates of 2D nucleation increase.

For heterogeneous 2D nucleation the energetics have been derived for cylindrical foreign particles oriented with the axis perpendicular to the terrace and with a radius R^s .¹¹ For this geometry, the energy barrier is given by:

$$\Delta G'_{2Dnuc(Het)} = \Delta G'_{2Dnuc} f(m, x),$$

(SI 6)

where $f(m, x)$ is a function of the angle, θ , by which the 2D nucleus wets the foreign particle:

$$m = \cos(\theta) = \frac{\gamma_{cs} - \gamma_{sw}}{\gamma_{cw}}$$

(SI 7)

and the ratio, x , between the sizes of foreign particles and the critical size of the 2D nucleus (r_c):

$$x = \frac{R^s}{r_c} = \frac{R^s k T \ln(\Omega)}{V \gamma_{cw}}.$$

(SI 8)

Values for $f(m,x)$ range from 1 to 0, decreasing with increasing values for x and m .¹¹ The outcome of these relationships is that heterogeneous 2D nucleation is highly promoted when surface free energies favour wetting of the foreign particle by the nucleus and when the size of the foreign particle is similar to or larger than the critical size of the 2D nucleus.

References

(1) Mørup, S.; Madsen, M. B.; Franck, J.; Villadsen, J.; Koch, C. J. W. A New Interpretation of Mössbauer Spectra of Microcrystalline goethite: “Super-Ferromagnetism” or “super-Spin-Glass” behaviour? *J. Magn. Magn. Mater.* **1983**, 40 (1–2), 163–174.

(2) Kanzaki, T.; Katsura, T. Mössbauer Spectra at 77 K of Products Formed during Transformation of Fe(OH)₂ to Fe₃O₄ in Aqueous Suspension by Air Oxidation. *J. Chem. Soc. Dalt. Trans.* **1986**, 6, 1243–1246.

(3) Cuttler, A. H.; Man, V.; Cranshaw, T. E.; Longworth, G. A Mössbauer Study of Green Rust Precipitates: I. Preparations from Sulphate Solutions. *Clay Miner.* **1990**, 25, 289.

- 237 (4) Christiansen, B. C.; Dideriksen, K.; Katz, A.; Nedel, S.; Bovet, N.; Sørensen, H.
238 O.; Frandsen, C.; Gundlach, C.; Andersson, M. P.; Stipp, S. L. S. Incorporation of
239 Monovalent Cations in Sulfate Green Rust. *Inorg. Chem.* **2014**, 53, 8887-8894.
- 240 (5) Christiansen, B. C.; Balic-Zunic, T.; Petit, P. O.; Frandsen, C.; Mørup, S.;
241 Geckeis, H.; Katerinopoulou, A.; Stipp, S. L. S. Composition and Structure of an Iron-
242 Bearing Layered Double Hydroxide (LDH) - Green Rust Sodium Sulphate. *Geochim.*
243 *Cosmochim. Acta* **2009**, 73, 3579-3592.
- 244 (6) Huminicki, D. M. C.; Hawthorne, F. C. The crystal structure of nikischerite,
245 $\text{NaFe}^{2+}_6\text{Al}_3(\text{SO}_4)_2(\text{OH})_{18}(\text{H}_2\text{O})_{12}$, a mineral of the shigaite group. *Can. Mineral.* **2003**, 41,
246 79-82.
- 247 (7) De Yoreo, J. J.; Vekilov, P. G. Principles of Crystal Nucleation and Growth. *Rev.*
248 *Mineral. Geochem.* **2003**, 54, 57-93
- 249 (8) Kashchiev, D.; van Rosmalen, G. M. Nucleation in solutions revisited. *Cryst. Res.*
250 *Technol.* **2003**, 38, 555 – 574.
- 251 (9) Vekilov, P. G. Nucleation. *Cryst. Growth Des.* **2010**, 10, 5007–5019.
- 252 (10) Sears, R. P. Nucleation: theory and applications to protein solutions and colloidal
253 suspensions. *J. Phys.: Condens. Matter* **2007**, 19, 033101.
- 254 (11) Liu, X. Y.; Maiwa, K.; Tsukamoto, K. Heterogeneous two-dimensional nucleation
255 and growth kinetics. *J. Chem. Phys.* **1997**, 106, 1870-1879.
- 256

257 **Figure Captions**

258 Figure SI1. PDF for precipitate formed by titrating an $\text{Al}_2(\text{SO}_4)_3$ solution to pH 7.

259 Figure SI2. Mössbauer spectra of LDH with $x_{\text{Al}} = 0, 0.03, 0.1$ and 0.2 with fitted
260 components. Patterns were scaled to yield identical absorption at $v = -0.1$ mm/s.

261 Figure SI3. The Me-Me peak position as a function of Fe(III)/Fe(II) molar ratio. Both
262 values were derived from peak fitting with Gaussian shaped contributions.

263 Figure SI4. Heron's formula describing the relationship between height and side lengths
264 for a right angled triangle.

265 Figure SI5. PDFs of variously curved single Me hydroxide sheets ($x_{\text{Al}} = 0.33$) calculated
266 with DiffPy-CMI. A 18 nm sheet based on the structure of Huminicki and Hawthorne⁶
267 were produced and bent with the software CrystalMaker. In the DiffPy-CMI calculations,
268 scale and cell dimension was first fit to the r range 1.7 to 8 Å of the measured PDF, to
269 have reasonably correct local structure. Then, the cell dimensions were fixed and only
270 scale were fitted to optimise agreement between measured and calculated data in the r
271 range 1.7 to 60 Å.

272 Figure SI6. Illustration of the structure of interlayer ions (top most) and hydroxides sheets
273 (located below interlayer ions) in A) $\text{GR}(\text{Na}, \text{SO}_4)$ and B) nikisherite. Oxygens are placed
274 at the apices of polyhedra.

275 Figure SI7. Illustration of the imposed displacement vector and its rotation.

276 Figure SI8. Measured and calculated patterns as well as the residual after fitting crystal
277 models to the data for A) GR(Na,SO₄) ($x_{Al} = 0$) and B) nikisherite ($x_{Al} = 0.33$).

278 Figure SI9. Aqueous Fe(II) concentration determined for LDH with $x_{Al} = 0$ and $x_{Al} =$
279 0.12. The red and black lines indicate the onset of oxidative transformation of LDH to
280 Fe(III)-oxyhydroxides based on changes in base addition rates.

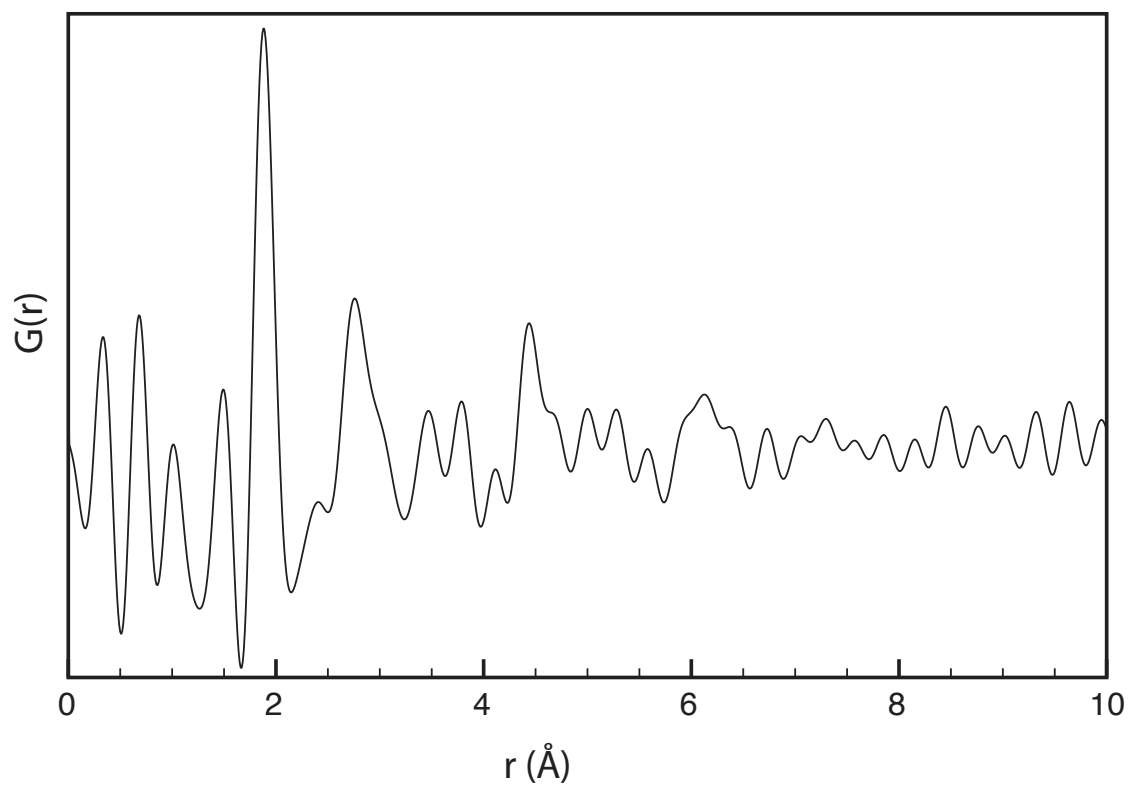


Figure SI1

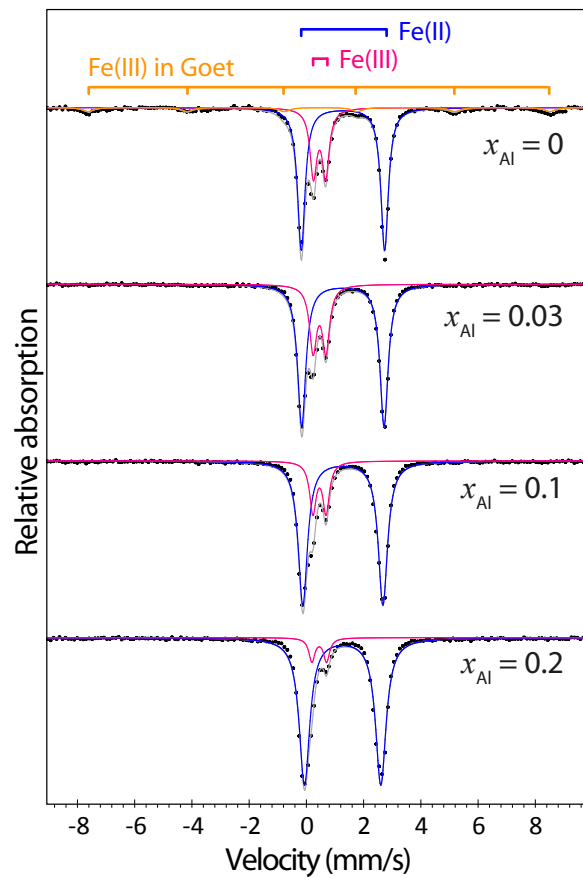


Figure SI2

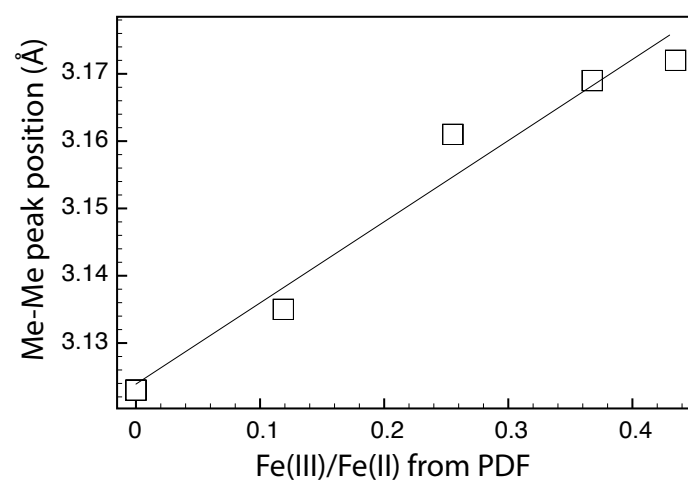
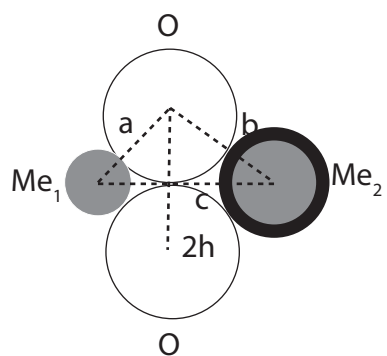


Figure S13

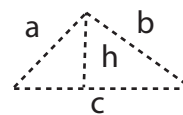


$$a = \text{Me}_1\text{-O}$$

$$b = \text{Me}_2\text{-O}$$

$$c = \text{Me}_1\text{-Me}_2$$

$$h = 1/2 \text{ O-O}$$



$$h^2 = b^2 - \left(\frac{-a^2 + b^2 + c^2}{2c} \right)^2$$

Figure SI4

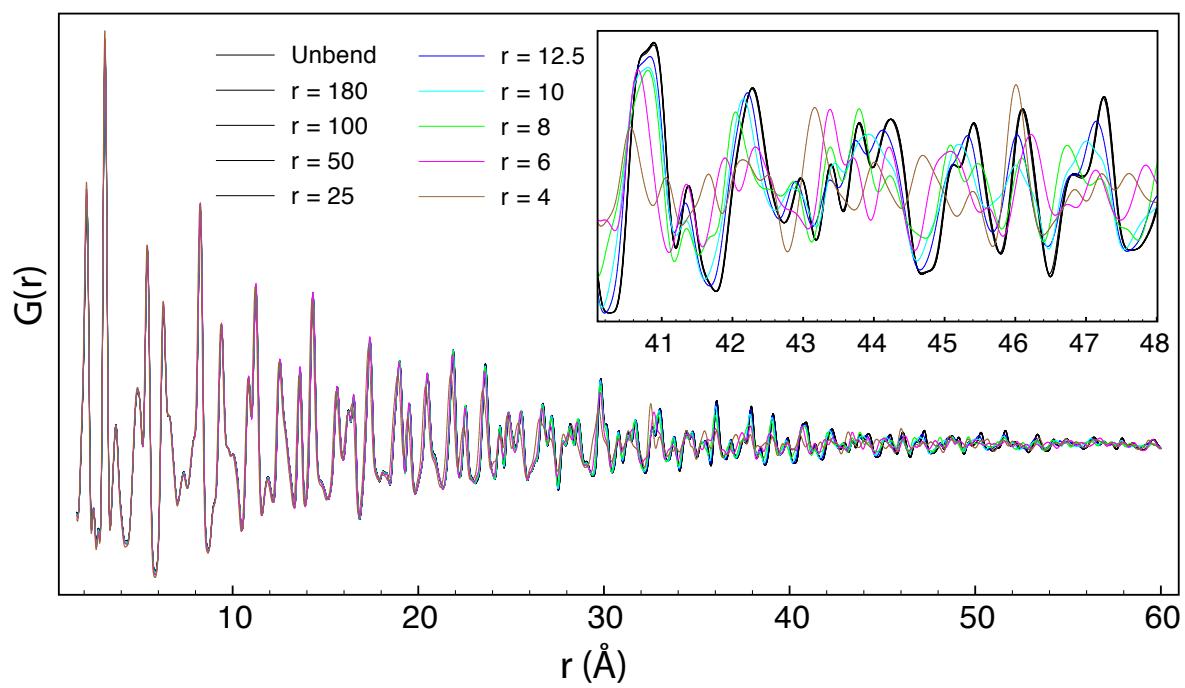


Figure S15

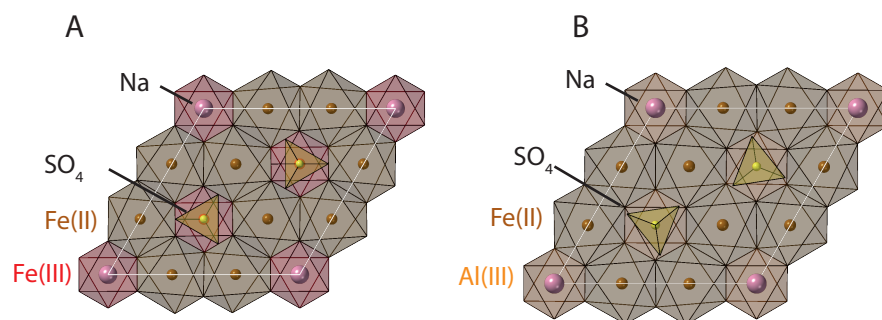
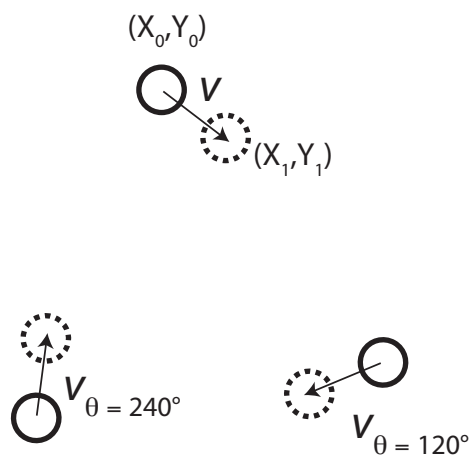


Figure SI6



$$\text{Vector } v = \begin{pmatrix} X_0 - X_1 \\ Y_0 - Y_1 \end{pmatrix} = \begin{pmatrix} \Delta X \\ \Delta Y \end{pmatrix}$$

$$\text{Vector } v_\theta = \begin{pmatrix} \Delta X \cos(\theta) - \Delta Y \sin(\theta) \\ \Delta X \sin(\theta) + \Delta Y \cos(\theta) \end{pmatrix}$$

- Original O atom
- ⊙ Displaced O atom

Figure SI7

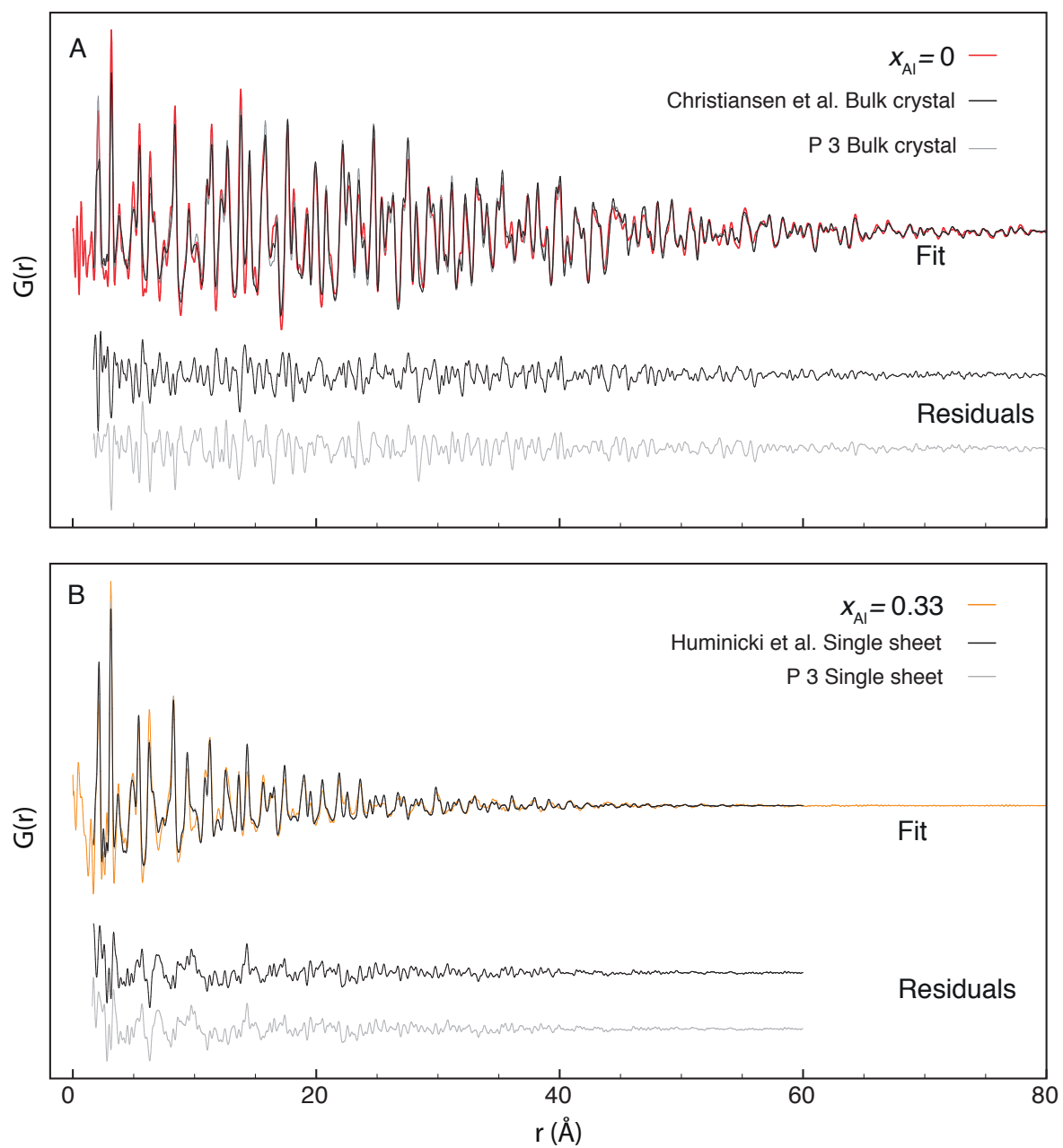


Figure S18

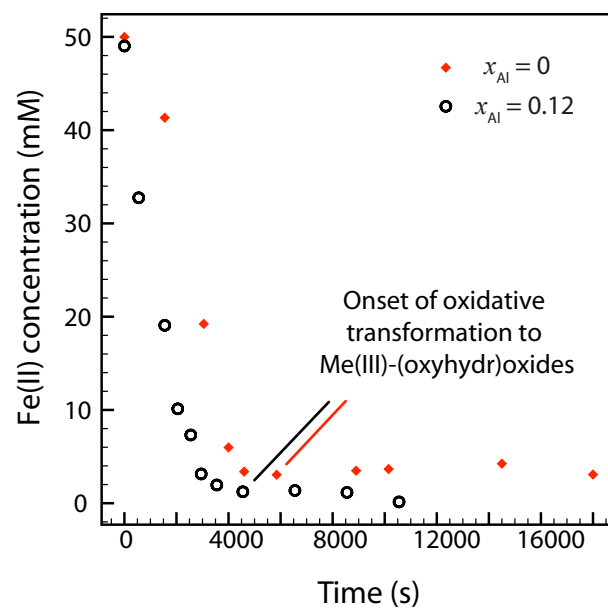


Figure S19